

₅₁₃ CHAPTER 4

₅₁₄ ANALYSIS

₅₁₅ In this chapter, the details of antiproton analysis will be given, including all the steps of
₅₁₆ deriving the time averaged and time dependent antiproton to proton flux ratio. To determine
₅₁₇ the flux ratio, the definition of flux should be given first. In general, the flux is calculated
₅₁₈ by:

$$\Phi(|R|) = \frac{N(|R|)}{\Delta R \cdot T(|R|) \cdot A(|R|) \cdot \epsilon(|R|)} \quad (4.1)$$

₅₁₉ where $N(|R|)$ is the event count numbers, ΔR is the rigidity bins, $T(|R|)$ is the measuring
₅₂₀ time, and the $\epsilon(|R|)$ is the trigger efficiency, $A(|R|)$ is the effective acceptance. All the
₅₂₁ rigidity should be the true rigidity of the event, while the event number from the template
₅₂₂ fit is obtained as a function of reconstructed rigidity. Therefore unfolding procedure should
₅₂₃ be done regarding this issue. This will be discussed further in section 4.8.

₅₂₄ In section 4.1, the data reconstruction and selection is discussed. Section 4.2 shows the
₅₂₅ construction of charge confusion estimator. Section 4.3 describes how the TRDlikelihood
₅₂₆ estimator is constructed. In section 4.4, the template fit procedures to get the antiproton
₅₂₇ signals in different rigidity ranges are shown. Section 4.5 gives the detail about how to
₅₂₈ calculate the effective acceptances of antiproton and proton. In section 4.6, the measuring
₅₂₉ time used in this analysis is determined. In section 4.7, the trigger efficiency used in this
₅₃₀ analysis is calculated. Section 4.8 shows the unfolding procedure. In section 4.9, the formula
₅₃₁ for calculation of antiproton to proton flux ratio is derived. In section 4.10, the different
₅₃₂ systematic uncertainties in different rigidity ranges are discussed.

533 **4.1. Data Selection**

534 **4.1.1. AMS-02 Data and Monte Carlo Simulation**

535 This section shows the data used in this analysis and the complete list of cuts and selections.
536 In this analysis, the used AMS-02 experiment data is collected from 20.May 2011 to 03.May
537 2021. Raw collected data need some calibration and alignment work and then could be
538 reconstructed via AMS-02 official software (named gbatch), resulting in the analysis data
539 stored in ROOT file format. The ROOT data analysis format is developed at CERN that is
540 dedicated for High energy particle physics analysis [88] . Furthermore, a software developed
541 in Aachen called ACSoft is used to generate data in a higher-level structure called ACQT
542 [89] . The analysis in this thesis is based on the pass7 version data (reconstructed via gbatch
543 in version B1130).

544 The rigidity bin used in this analysis is the same as the one used in the previous AMS-02
545 proton analysis [90] , which is determined by rigidity resolution. In rigidity higher than 80.5
546 GV, the rigidity bins are merged in every two bins to increase antiproton statistics.

547 The sun is not a solid body but is made of gas plasma. Due to the solar rotations, different
548 latitudes would show different rotation periods. From the view of the Earth, the solar
549 rotations can be quantified with the Bartels Rotation Numbers. The Bartels Rotation
550 Numbers is exactly 27 days, close to the synodic rotation period [91] . The starting counting
551 was from 8th Feb 1832, and this day was arbitrarily assigned by Julius Bartels.

552 For time dependent analysis, the collected ISS data is divided into six Bartels Rotations
553 time bins. Because of the rigidity cutoff, the statistic in the low rigidity range in each
554 time interval is limited. Therefore, the rigidity bins are merged in every two original time
555 averaged rigidity bins in time dependent antiproton analysis. The data collection used in
556 this thesis started in May 2011, which is Bartels Rotation 2426, and ended in May 2021,
557 which is Bartels Rotation 2561. In total, the data can be divided into 23 intervals of six
558 Bartels Rotations though the last time bin has less data than the full six Bartels Rotations.

559 Due to the technical problems in tracker pumps and a repair mission for new TTCS systems
560 from Nov 2019 to Jan 2020, the operation mode frequently changed during some periods
561 and the tracker had to turn off. In those periods, the data taking was excluded and not
562 used in this analysis.

563 To validate the sub detector's performance and study the detector's operation, an extensive
564 set of MC simulations has been done by the AMS-02 collaboration with the help of the
565 Geant4 framework [92, 93] . This includes the interaction with all the sub-detectors and
566 their support structure. In this thesis, all the AMS-02 MC events are generated from the
567 top of the experiment with a 3.9 meters plane, the solid angle of the generated event is $\pi \cdot \text{sr}$,
568 and the generated momentum spectrum is either a power law with spectrum index -2.7 or
569 a constant in $\log(p)$ axis. By comparing the data distributions in different variables, the

570 sub-detectors response for different cosmic rays can be systematically studied.

571 In this thesis, the used MC datasets are protons, antiprotons, and electrons. They are
572 generated in different momentum ranges for various purposes. For example, one of the main
573 purposes of using MC proton data in this analysis is to study proton charge confusion, which
574 is proton events but measured with the wrong rigidity sign. The reasons are finite tracker
575 rigidity resolution and the interactions with the sub-detectors [94]. By selecting the negative
576 rigidity data samples from the proton MC dataset, the proton charge confusion data can be
577 selected. More detail will be discussed in 4.2. Some other usages like calculating effective
578 acceptance and determining the systematic uncertainties due to acceptance will be shown
579 in detail later in this chapter.

580 For the simulated MC events, the generated momentum spectrum does not perfectly match
581 the realistic spectrum. This could introduce bias in some variable distributions in MC. In
582 order to correct this, the weight of MC events should be reassigned by calculating the ratio
583 of event counts over reference flux. For example, the re-weighting of the proton MC dataset
584 uses AMS-02 published proton flux result [90] as reference flux. The re-weighting factor
585 can be obtained by dividing the MC event count by reference event counts in each rigidity
586 bin. The acquired re-weighting factor will be used in filling variable histograms for further
587 procedure.

588 Up to May 2021, the AMS-02 experiment has collected more than 174 billion cosmic rays
589 events. To select antiproton events from them, cuts and selections must be put on first.
590 There are two levels of selection, the first is the preselection, and the second is the selection.
591 In the next few subsections, the definition of all selections and passing ratios will be given.

592 4.1.2. Preselection Cuts

593 The first level of cuts and selections is preselection. The purpose is to discard data taken in
594 bad sub-detectors operations or in bad quality. These selections are general and should be
595 applied before any cosmic ray component analyses. The preselection consists of two parts:
596 data taking quality cuts and analysis data quality cuts.

597 Data taking quality cuts require all the sub-detectors running in nominal conditions, and
598 the data taking condition is normal. The first one excludes the period that any sub-detector
599 has some special operations or tests. For example, the TRD gas refill takes place around
600 every month. In this period, the data taken is not included in this analysis. The second
601 one requires that the data taking period is normal. For instance, if the ISS is in the South
602 Atlantic Anomaly (SAA) area, the data taken in this period is not included in this analysis.
603 In summary, the table of 4.1 shows the pass ratio of all the data taking quality cuts.

604 After the data taking quality cuts, all the pass data are taken in the normal operation period.
605 But for analysis, further quality selections are needed to ensure the analysis based on these
606 data is meaningful. The analysis data quality cuts are used to discard the low quality

Table 4.1: List of data taking quality cuts

Cuts	Description	Pass Ratio
Bad Runs	Remove events in bad sub-detector status	99.73 %
Second Within Run	Remove events without a run ID	99.92 %
Bad Reconstruction Period	Remove events with bad reconstruction efficiency	95.15 %
Bad Facing Angle	Remove events in rotated ISS status	99.78 %
No Missed Events	Remove seconds with more than 10% events missing	99.91 %
Bad Live Time	Remove seconds with live time fraction (see section 4.6) < 0.5	95.67 %
Too Many Events In Second	Remove seconds with too many events	97.86 %
Good Alignment	Remove events without good alignment	99.86 %
High TRD Occupancy Period	Remove events with too high TRD occupancy	97.80 %
No Hardware Errors	Remove events with hardware errors	99.91 %

607 collected data then the analysis is based on relatively golden data. In 4.2, the complete list
 608 of analysis data quality cuts and the correspondent pass ratios are shown.

Table 4.2: List of analysis data quality cuts

Cuts	Pass Ratio
Has TOF Beta Measurement	68.02 %
Particle is Downgoing	88.03 %
Has Hits in Central Inner Tracker	70.16 %
Has Single Tracker Track	61.01 %
Tracker Track Fit Chi2 in X	97.33 %
Tracker Track Fit Chi2 in Y	90.64 %
Has Hits in all four TOF Layers	89.44 %

- 609 • The **Has TOF Beta Measurement** requires that the TOF beta measurement is
 610 available. The TOF beta is used to separate antiproton signals and backgrounds in
 611 low rigidity ranges.
- 612 • The **Particle is Downgoing** is the cut on particle going direction. By requiring
 613 TOF beta measurement is positive, the particle going from upper TOF to lower TOF
 614 is selected.
- 615 • The **Has Hits in Central Inner Tracker** requires hits in tracker layer 3 or 4, 5 or 6,
 616 7 or 8. To have an accurate rigidity measurement, the tracker hits inside the magnet
 617 is necessary. Therefore central inner tracker should have enough hits to construct the
 618 rigidity.
- 619 • The **Has Single Tracker Track** requires that for each event, only one reconstructed

620 tracker track is found. To avoid multiple tracker tracks produced by interaction, this
621 analysis only uses single tracker track events.

- 622 • The **Tracker Track Fit Chi2 in X** and **Tracker Track Fit Chi2 in Y** are the cuts
623 on tracker track fit Chi2 less than 10 in X and Y directions respectively. To ensure
624 the events used for analysis have good tracker track fit and rigidity correspondently,
625 the cuts on Chi2 in bending and unbending directions are mandatory.
- 626 • The **Has Hits in all four TOF Layers** requires that all the four TOF layers have
627 hits. Since the TOF provides trigger and also the beta measurement, hits on all four
628 TOF layers give a precise response of TOF.

629 **4.1.3. Quality Cuts**

630 The preselection is independent of the analysis topic. For the antiproton to proton ratio
631 analysis, some dedicated selections need to be applied further. These cuts are mainly used
632 to select charge one particle and ensure good quality analysis events. To have good quality
633 analysis variables like particle charge or beta, the basic reconstruction of events needs to be
634 done with the minimum response of sub-detectors. In 4.3, the table shows all the selections
635 used in this analysis.

Table 4.3: List of quality cuts

Cuts	Pass Ratio
Tracker Charge Cut	87.16%
Upper TOF Charge Cut	97.46%
Lower TOF Charge Cut	97.22%
TRD Number Of Raw Hits Cut	98.89%
TRD Active Layers Cut	90.71%
Tracker Track In Trd Acceptance Cut	87.48%
TRD TOF Track Match XY Cut	96.76%

- 636 • The **Tracker Charge Cut** is the cut on the inner tracker charge measurement. With
637 the cut $0.7 < \text{inner tracker charge} < 1.3$, the charge one particle is selected from the
638 tracker. In the low rigidity analysis, the hits on the tracker track L1 and L9 are not
639 required. Therefore only the charge measurement in the inner tracker is guaranteed.
- 640 • The **Upper TOF Charge Cut** is the cut on upper TOF charge measurement. The
641 lower value is 0, which cuts away the bad charge reconstruction events, and the higher
642 value is 1.5, which cuts away charge two and higher events.
- 643 • The **Lower TOF Charge Cut** is the cut on lower TOF charge measurement. The
644 lower limit is 0 and the higher limit is 2. Due to the possible interaction between the
645 two TOF layers, the cut value on lower TOF is wider than on upper TOF.
- 646 • The **TRD Number Of Raw Hits Cut** requires $8 < \text{TRD Number Of Raw Hits} <$

647 1000. To have a minimum response of TRD, the minimum cuts on TRD raw hits are
648 necessary. This ensures a good reconstruction of TRD variables.

- 649 • The **TRD Active Layers Cut** requires $14 < \text{TRD Active Layers} < 20$. To ensure
650 a good TRD measurement of the event and construct the **TRDLikelihood** precisely, a
651 minimum of TRD active layers is required.
- 652 • The **Tracker Track In Trd Acceptance Cut** requires that the tracker track of the
653 event is inside TRD's geometrical acceptance. Therefore, the tracker track produced
654 from the side or from interaction could be reduced.
- 655 • The **TRD TOF Track Match XY Cut** cut on the distance between the TRD track
656 and the TOF track less than 40 cm. This ensures that the TRD track and TOF track
657 are consistent with each other and a clean traverse path is obtained.

658 4.2. Charge Confusion Estimator

659 Due to the finite rigidity resolution or the interactions with the AMS sub-detectors, protons
660 could be misconstrued with opposite rigidity signs. This is called "Charge Confused Pro-
661 tons". The charge confused protons can mimic the behavior of charge correct antiprotons.
662 Therefore, the charge confused protons can go into the antiproton signal ranges when de-
663 termining the antiprotons. With the rigidity going up, the wrongly reconstructed protons
664 increase dramatically. So in the high rigidity range, most backgrounds of antiproton signals
665 are charge confused protons.

666 To solve this problem, the machine learning technique is used. The separation of antiproton
667 signals and charge confused protons depends on the sign of rigidity. Since there are only
668 two possible categories: positive rigidity and negative rigidity, the case falls into a binary
669 classification. After checking the data/MC matching, the proton MC simulation data can
670 be used in this learning process. In summary, the charge confusion proton case is supervised
671 learning with two categories.

672 To train the charge confusion classifier estimator, variables containing relevant information
673 should be used. In this analysis, 16 variables from the sub-detectors are used for training.
674 Most variables are from the tracker, and the others are from the TOF and the TRD. These
675 variables are constructed by summarising the characters of charge confused proton events
676 and are also used in previous AMS-02 antiproton analyses [50] .

677 The training samples are taken from proton MC simulation. By selecting the negative
678 rigidity events from proton MC data in the absolute rigidity above around 20 GV, the
679 charge confused protons can be obtained. Since the antiproton and proton only have charge
680 differences, the antiproton's behavior in sub-detectors is assumed to be the same as the
681 proton's, but only the rigidity sign is opposite. The charge correct antiproton samples can
682 be replaced by charge correct proton samples but with opposite rigidity signs.

683 In the appendix A, the complete list of all the 16 variables and their definitions are shown.
 684 In figure 4.1, the four most important variables and their responses are given as examples
 685 to illustrate the information of separating the charge correct signal and charge confused
 686 background.

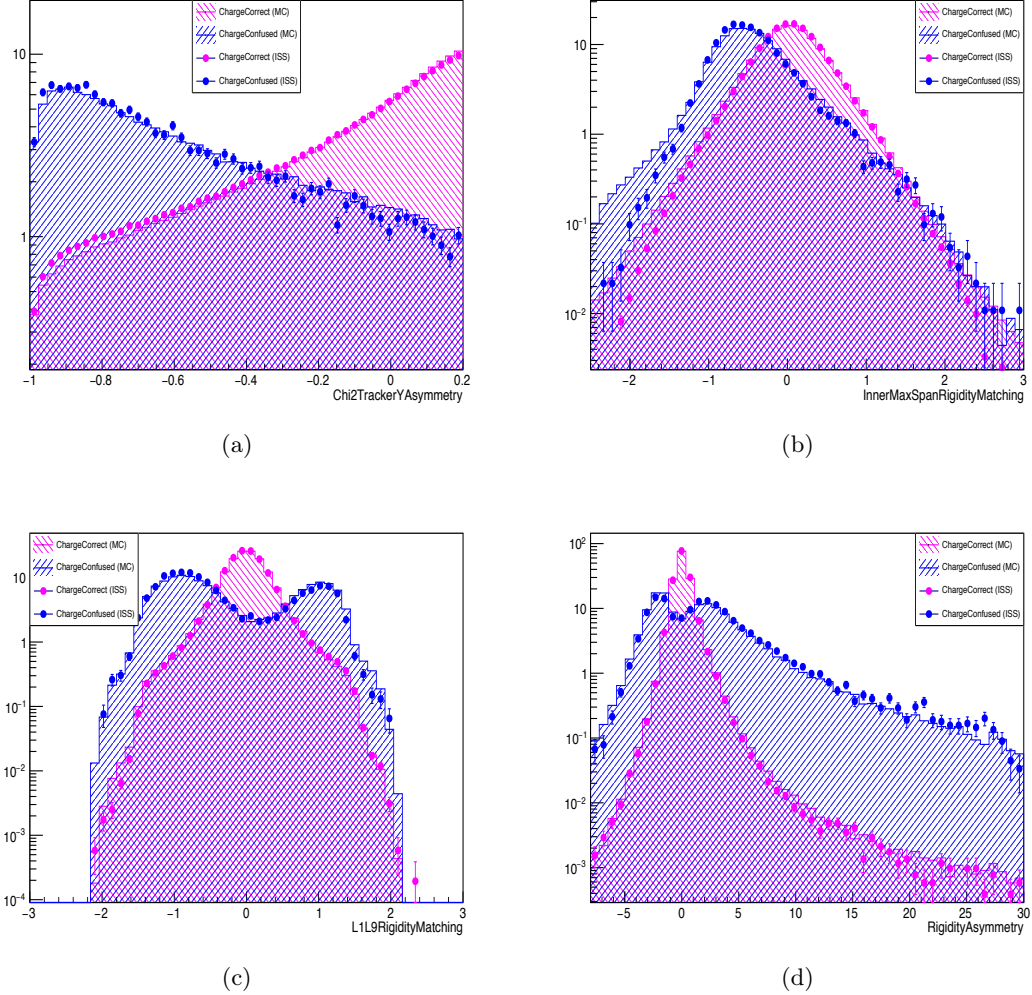


Figure 4.1: Four most important input variables used for training the charge confusion estimator: a). Chi2TrackerYAsymmetry b). InnerMaxSpanRigidityMatching c). L1L9RigidityMatching d). RigidityAsymmetry. The points are collected data, and the histograms are proton MC simulation. The pink is the distribution for the charge correct antiprotons, and the blue is the distribution for the charge confused protons.

687 The definitions of the four variables are given here:

688 1 **RigidityAsymmetry** = $\frac{\text{RigidityInnerL1} - \text{RigidityInnerL9}}{\text{RigidityInnerL1} + \text{RigidityInnerL9}}$. The RigidityInnerL1 is the rigid-
 689 ity reconstructed with only the hits in the inner tracker layers and tracker layer 1. The
 690 RigidityInnerL9 is the rigidity reconstructed with only the hits in the inner tracker

691 layers and tracker layer 9.
 692 2 **Chi2TrackerYAsymmetry** = $\frac{\text{Chi2TrackerYInner} - \text{Chi2TrackerY}}{\text{Chi2TrackerYInner} + \text{Chi2TrackerY}}$. The Chi2TrackerYInner
 693 is the Chi2 of the Y side tracker track fitting only from the inner tracker layers. The
 694 Chi2TrackerY is the Chi2 of the Y side tracker track fitting from all the tracker layers.
 695 3 **InnerMaxSpanRigidityMatching** = $100 \cdot \left[\left(\frac{1.0}{\text{RigidityInner}} \right) - \left(\frac{1.0}{\text{Rigidity}} \right) \right] \cdot \frac{R}{|R|}$. The
 696 RigidityInner is the rigidity reconstructed only with the hits in the inner tracker layers.
 697 The Rigidity is the rigidity reconstructed with the hits in all the tracker layers.
 698 4 **L1L9RigidityMatching** = $100 \cdot \left[\left(\frac{1.0}{\text{RigidityInnerL1}} \right) - \left(\frac{1.0}{\text{RigidityInnerL9}} \right) \right] \cdot \frac{R}{|R|}$. The Rigid-
 699 ityInnerL1 and RigidityInnerL9 have been defined in the previous value.
 700 From the figure, we could see that the data and MC have similar distributions. This is
 701 important for further steps. The estimator training process is based on MC data. In order
 702 to make sure the trained estimator is applicable for data, the distributions of MC and data
 703 have to match with each other.
 704 All four variables contain information about the differences between signal and background.
 705 From the figure, the differences between signal distribution and background distribution are
 706 easy to observe. These differences are used for the further training process.
 707 In the TMVA framework [95], there are different training methods provided, like Boosted
 708 Decision Tree (BDT), Support Vector Machine (SVM), Gradient Tree Boosting (GTB), or
 709 Likelihood method. To achieve the best separation performance, all the methods have been
 710 tried to get the best separation power. In this analysis, the Boosted Decision Tree (BDT)
 711 is used as the default method since it provides the best separation between signals and
 712 backgrounds.
 713 The proton MC data is divided into positive and negative parts with the same amount of
 714 events. Each part is divided into train sample, validation sample, and test sample with
 715 a ratio of 6:3:1. To avoid overtraining, the training process requires the response on the
 716 training sample should be the same as the response on the validation sample.
 717 After training, the *charge confusion estimator* is obtained. In figure 4.2, the separation
 718 between charge correct antiproton signals and charge confused proton backgrounds in an
 719 example rigidity bin of 147-175 GV can be seen. The peak at 1 means the charge correct
 720 events, and the peak at 0 means the charge confused events. By setting a cut on the charge
 721 confusion estimator, the charge correct antiproton samples can be obtained. But in this way,
 722 some antiproton signals would still be lost and some backgrounds go into the signal range.
 723 Therefore, a template fit method is required to get the signal numbers precisely. This will
 724 be shown in section 4.4.

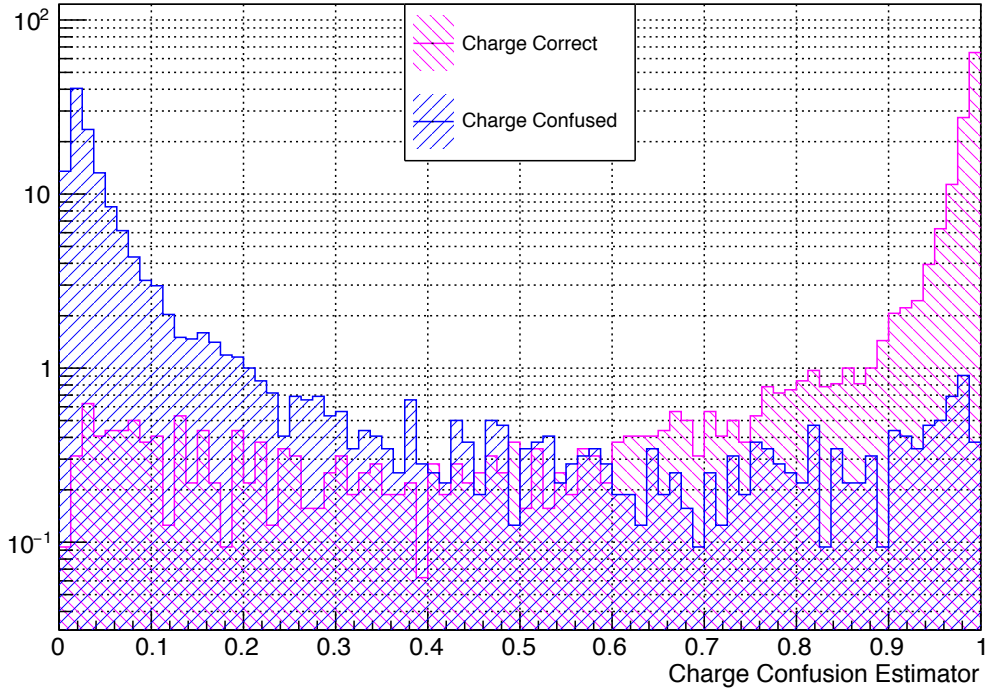


Figure 4.2: The charge confusion estimator response on charge correct antiprotons (pink) and charge confused protons (blue) in 147-175 GV

725 4.3. TRD Estimator

726 Except for the charge confusion estimator, another estimator to be constructed before the
 727 antiproton signal determination is the TRDLikelihood estimator. The charge confusion
 728 estimator is constructed to separate charge confused protons backgrounds, while the TRD-
 729 Likelihood estimator is constructed to separate light particle backgrounds like electrons.

730 As introduced in section 3.2, the TRD sub-detector has the power to separate the heavy and
 731 light particles. When the protons (antiprotons) pass the tubes of TRD, they leave dE/dX
 732 signals. For the electrons, due to the high Lorenz factor, they emit transition radiation,
 733 which can be used to distinguish between electrons and protons (antiprotons).

734 In the maximum likelihood method, the energy deposit distributions in TRD are normalized
 735 and used as the probability distributions for each hit: $p^k(E_{dep})$. Then the signals from the
 736 20 layers are combined to construct a likelihood \mathcal{L} for each particle specie:

$$\mathcal{L} = \sqrt[n]{\sum_{k=1}^n P^k(E_{dep})} \quad (4.2)$$

737 For example, for electron and proton, \mathcal{L}_e and \mathcal{L}_p are constructed. According to Neyman-
 738 Pearson lemma [63], the separation power can reach maximum in the form of the log-
 739 likelihood ratio. Therefore, the TRD estimator is defined as:

$$\Lambda_{TRD} = -\log\left(\frac{\mathcal{L}_A}{\mathcal{L}_A + \mathcal{L}_B}\right) \quad (4.3)$$

740 If A = electron and B = proton, then the likelihood is called **TRDLikelihood**, which provides
 741 separation power for electron and proton. In figure 4.3, the TRD estimators for electron and
 742 proton are shown. The two kinds of particles can be very well separated in this estimator,
 743 as shown in this figure.

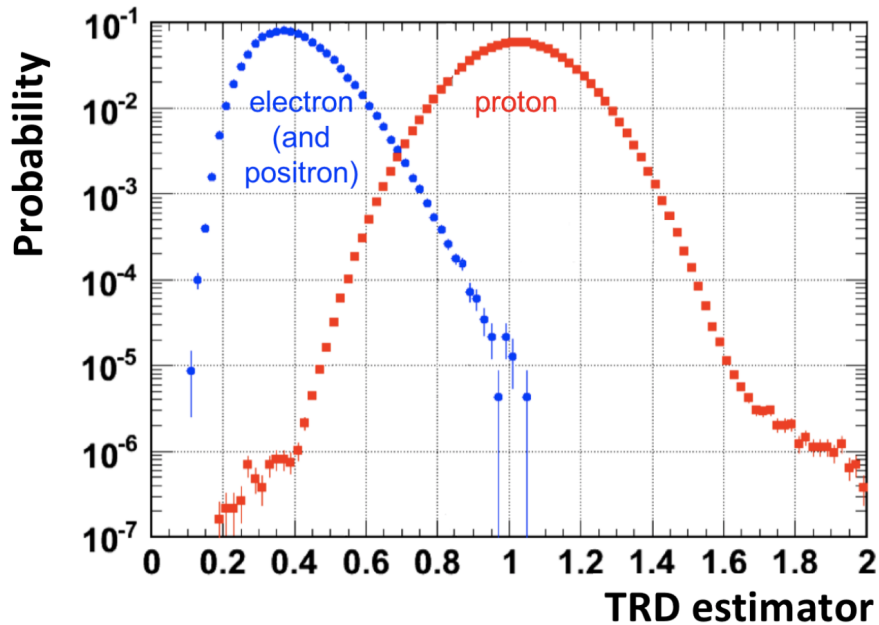


Figure 4.3: Separation between the electrons and protons in **TRDLikelihood** estimator. [58]

744 4.4. Template Fit

745 In this section, the template fits are shown in detail for time averaged analysis and time
 746 dependent analysis respectively. For different rigidity ranges, the template fits are different
 747 due to sub-detector resolutions and background contributions. The selections used to get the
 748 signal and background templates will be discussed, and then the template fit result will be
 749 shown. In time dependent analysis, the template fit and the result in six Bartels Rotations
 750 will be given.

751 4.4.1. Time averaged analysis

752 The first ingredient to construct the antiproton to proton flux ratio is the event number.
753 Due to the background level is not ignorable, cut-based analysis is not enough to get clean
754 signals. Therefore, to get the clean signals, the template fit method is needed in this analysis
755 to extract antiproton signals.

756 In different rigidity ranges, the detector resolutions and background components are differ-
757 ent. The whole analysis is divided into three independent parts: low rigidity range (1.0 GV
758 to 6.5 GV), intermediate rigidity range (3.0 to 19.5 GV), and high rigidity range (14.1 to
759 525 GV). The ranges are used as the same as the one in the previous AMS-02 antiproton
760 analysis [50] . In each range, a dedicated template fit method is used to get antiproton
761 signals.

762 Low Rigidity Range

763 In the low rigidity range, most backgrounds are electrons and interaction secondary particles
764 like pions. The TOF beta can be used to separate antiprotons and backgrounds because
765 of the different velocities of light particles and antiprotons in the low rigidity range. With
766 the rigidity going up, the separation power from TOF beta decrease, and at the same time,
767 the TRD separation power increase, so the TRDLikelihood can take over afterward in the
768 intermediate rigidity range. A 2D temple fit in TRDLikelihood and TOF beta is used in the
769 low rigidity range to have a smooth and stable separation power. The range in low rigidity
770 is from 1.0 GV to 6.5 GV. The lower limit is due to the low statistics after the geometrical
771 cutoff, and the higher limit is due to TOF beta resolution.

772 After cuts and selections, there are three major components in the data: antiprotons, elec-
773 trons, and secondaries. The three templates must be constructed first to do the template
774 fit. The antiproton template is taken from ISS positive rigidity data since the clean proton
775 data is easy to extract from it, and the rigidity sign does not impact the absolute value
776 of TOF beta and TRDLikelihood. The electron and the secondaries templates are taken
777 from the ISS negative rigidity data. To get the clean electron and secondaries from it,
778 dedicated selections should be applied respectively. Furthermore, after the preselection and
779 selection introduced in section 4.1, the negative rigidity data to be fitted should be selected
780 dedicatedly in the low rigidity range. In table 4.4 the full list of selections is shown.

781 In the table of 4.4, most cuts and selections are set with fixed value, while the TOFBetaCut:
782 $\beta_{low}(R) < \frac{1}{\beta} - \frac{1}{\sqrt{(R^2)/(m_p^2 + R^2)}} < 0.3$, and TRDLikelihoodCut: $\Lambda_{low}(R) < \text{TRDLogLikelihood} <$
783 1.7 are not. These two cuts are the template fit ranges, and the lower edge is rigidity-
784 dependent. By varying the lower edge of the template fit range, the systematic uncertainty
785 of the template fit can be evaluated. This will be discussed further later in section 4.10. For
786 the representative result, the template fit is performed at 90% signal efficiency. The rigidity
787 dependent lower edges are shown in figure 4.4.

Table 4.4: List of selections for templates

Antiproton template	Electron Template
TOFBetaCut	TOFBetaCut
TRDLikelihoodCut	TRDLikelihoodCut
$\text{TRDLikelihood}_{\text{P/He}} < 0.1$	β_{RICH} in RichAgl
TRDVTracksSize=1	$\beta_{RICH} - \frac{-R}{\sqrt{m_e^2 + R^2}} > -0.002$
TRDNumberOfHits<40	TRDSegmentsXZ=1
	TRDSegmentsYZ=1
	TRDNumberOfHits<35
Secondaries Template	Data Selection
TOFBetaCut	TOFBetaCut
TRDLikelihoodCut	TRDLikelihoodCut
β_{RICH} in RichAgl	$\text{TRDLikelihood}_{\text{P/He}} < 0.1$
$ \beta_{RICH} - \frac{-R}{\sqrt{m_\pi^2 + R^2}} < 0.002$	TRDSegmentsXZ=1
TRDSegmentsXZ>1	TRDSegmentsYZ=1
TRDSegmentsYZ>1	
TRDNumberOfHits>50	

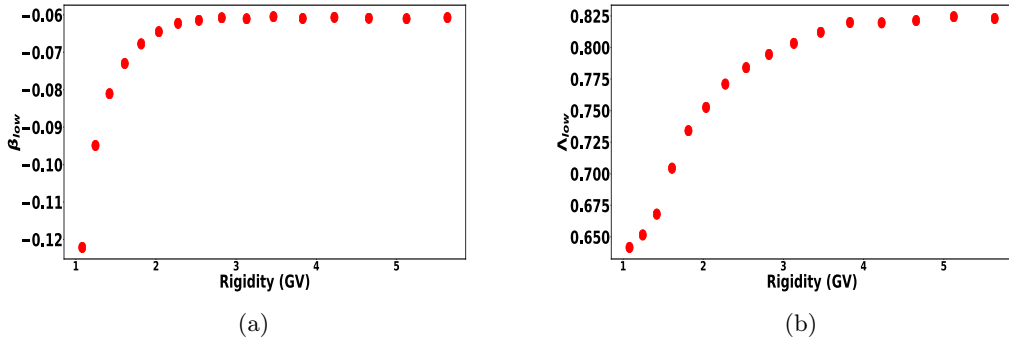
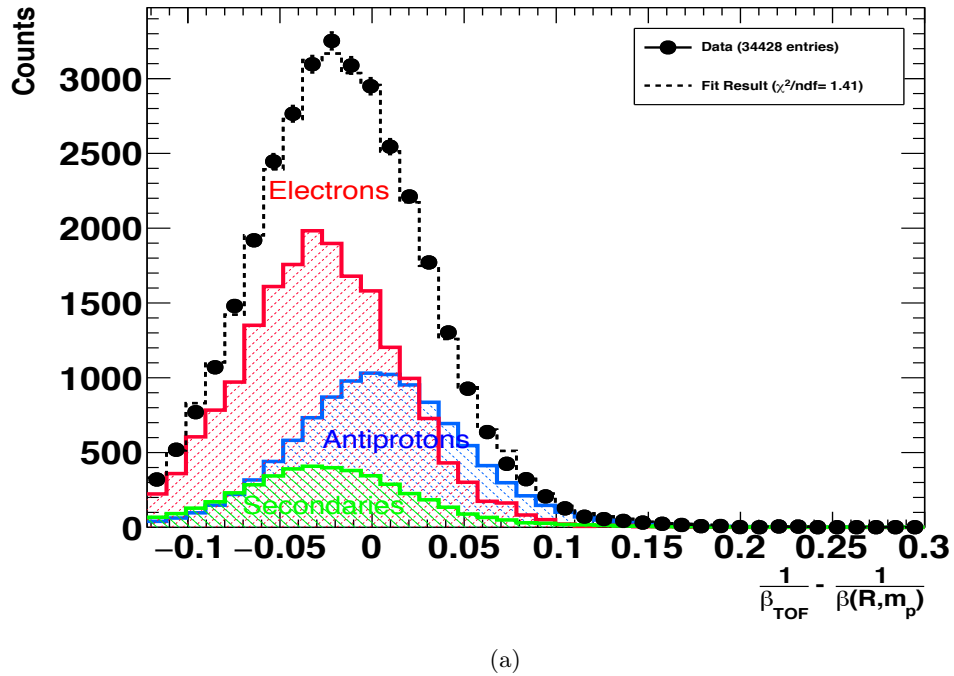
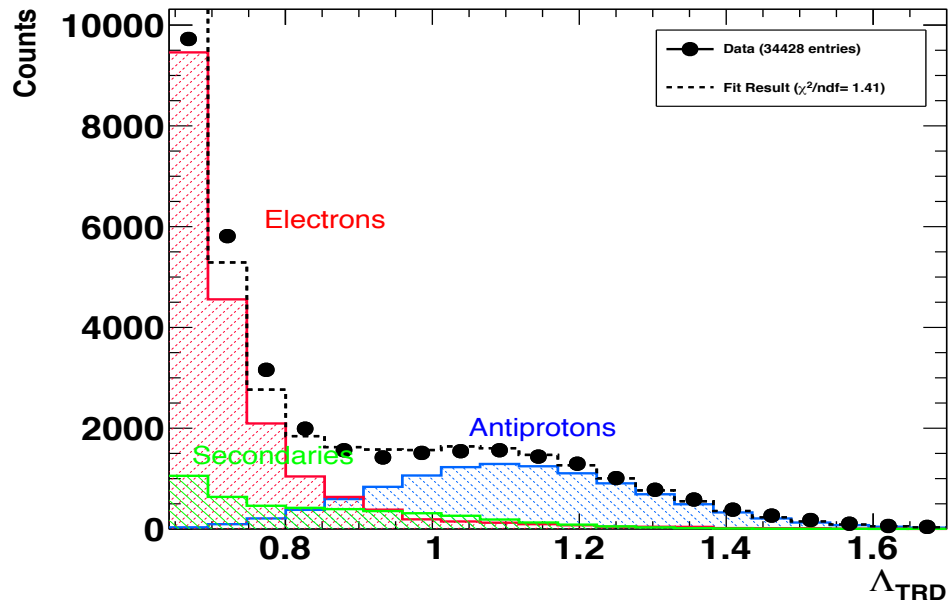


Figure 4.4: The rigidity-dependent lower edge of template fit range for 90% signal efficiency.
a). Lower edge for TOFBeta. b). Lower edge for TRDLikelihood.

788 In figure 4.5, the two projections of an example template fit in 3.64-4.02 GV are shown. The
789 three templates are interaction secondaries, electrons, and antiproton signals.



(a)



(b)

Figure 4.5: Example template fit in 3.64 to 4.02 GV in low rigidity range. a). $1/\text{TOFBeta}$ projection. In this projection, the value is subtracted by the $1/\beta$ with the assumption of antiproton mass, so the distribution can be normalized to be around 0. b). TRDLikelihood projection

790 The fit result gives the antiproton numbers in the low rigidity range. In figure 4.6 the
791 antiproton number obtained is given. The Chi2/dof of the correspondent template fit is
792 given in figure 4.7.

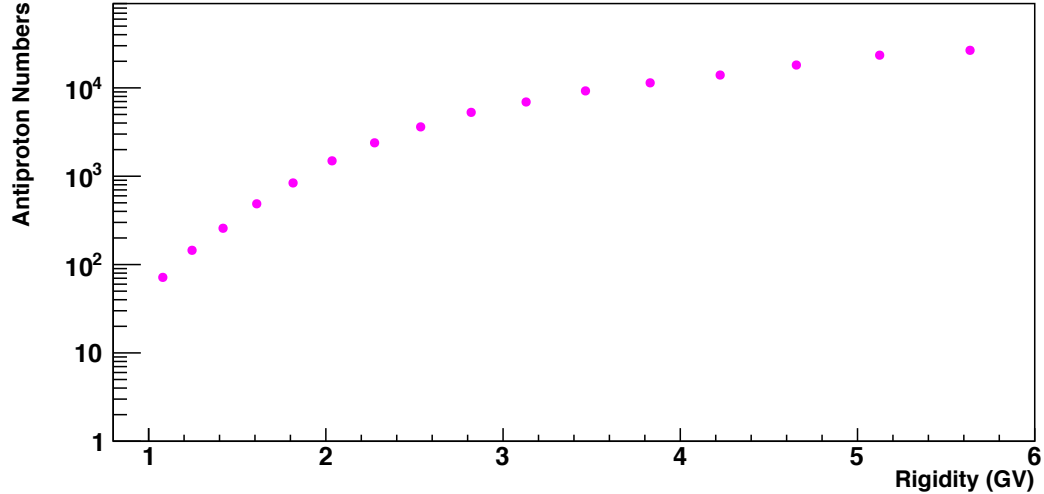


Figure 4.6: The antiproton numbers obtained from the template fit in low rigidity range

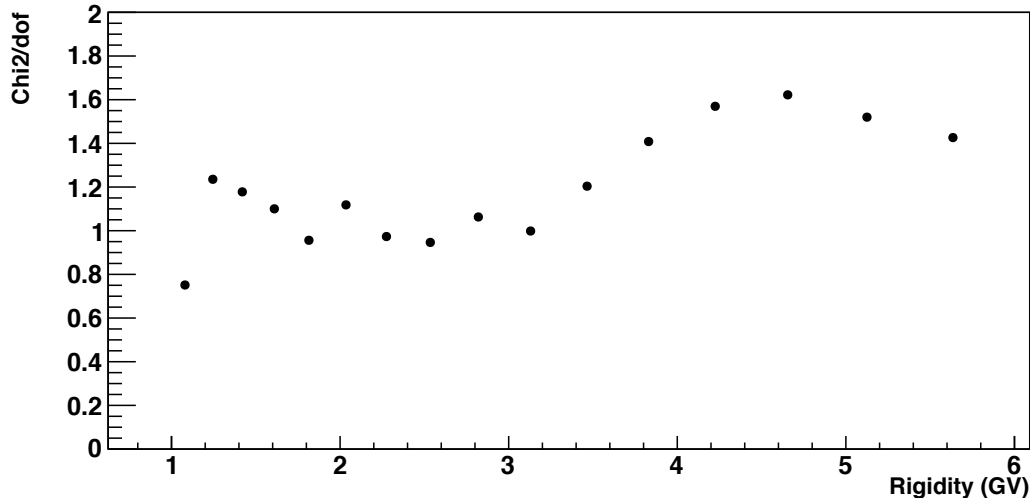


Figure 4.7: The Chi2/dof of template fit in low rigidity range

793 Intermediate Rigidity Range

794 In the intermediate rigidity range, the TOF Beta and TRDLikelihood 2D template fit is
795 replaced by a 1D template fit in TRDLikelihood since the separation power of TOF Beta

796 decreases with the rigidity going up and provides little power in this rigidity range. Above
 797 20 GV, the component of charge confused protons gradually increases, so it has to be added
 798 as an additional template. Therefore the 1D template fit can only be implemented up to
 799 around 20 GV.

800 In the intermediate rigidity range, the interaction secondaries component is ignorable. There-
 801 fore, the templates in this rigidity range are only antiprotons and electrons. Like the tem-
 802 plate fit in the low rigidity range, the templates are also taken from ISS data. The antiproton
 803 is taken from positive rigidity data, and the electron template is taken from negative rigidity
 804 data. The dedicated selections for data in the intermediate rigidity range are applied before
 805 the template fit. In table 4.5, the full list of selections to get templates and data selections is
 806 given. The TRDLikelihoodCut: $-2.0 < \Lambda_{TRD} < \Lambda_{high}(R)$ represents the template fit range,
 807 and the rigidity dependent $\Lambda_{high}(R)$ has the same absolute value as the lower edge in the low
 808 rigidity range but opposite sign. To avoid the light particle background, the RichBetaCut:
 809 $\beta_{RICH} < \beta_{high}(R)$ is also applied to restrict in signal range. The $\beta_{high}(R)$ is determined by
 810 90% signal efficiency. The ECALBDT is a value trained with ECAL response variables to
 811 separate protons and electrons. By applying a cut of 0.5 on ECALBDT, a clean electron
 812 sample can be obtained.

Table 4.5: List of selections for templates

Antiproton template	Electron Template	Data Selection
TRDLikelihoodCut	TRDLikelihoodCut	TRDLikelihoodCut
RichBetaCut	TRDNumberOfHits<35	RichBetaCut
TRDSegmentsXZ=1	ECALBDT>0.5	TRDSegmentsXZ=1
TRDSegmentsYZ=1	TRDSegmentsXZ=1	TRDSegmentsYZ=1
	TRDSegmentsYZ=1	

813 In figure 4.8, an example template fit of 10.1-11 GV is shown. The antiproton signals can
 814 be separated well with electron backgrounds.

815 The obtained antiproton number from the template fit is shown in figure 4.9. The corre-
 816 spondent Chi2/dof in intermediate rigidity range is given in 4.10.

817 High Rigidity Range

818 In the high rigidity range, the contribution of charge confusion protons increases with the
 819 rigidity going up. Therefore, the charge confusion estimator trained in section 4.2 should be
 820 used to separate antiprotons and charge confused protons. For electron separation, the TRD
 821 provides separation power, like in the low and intermediate rigidity range. In summary, a
 822 2D template fit in charge confusion estimator and TRDLikelihood estimator is performed
 823 in this range to get the antiproton signal.

824 In the 2D template fit, the three templates are antiprotons, electrons, and charge confused

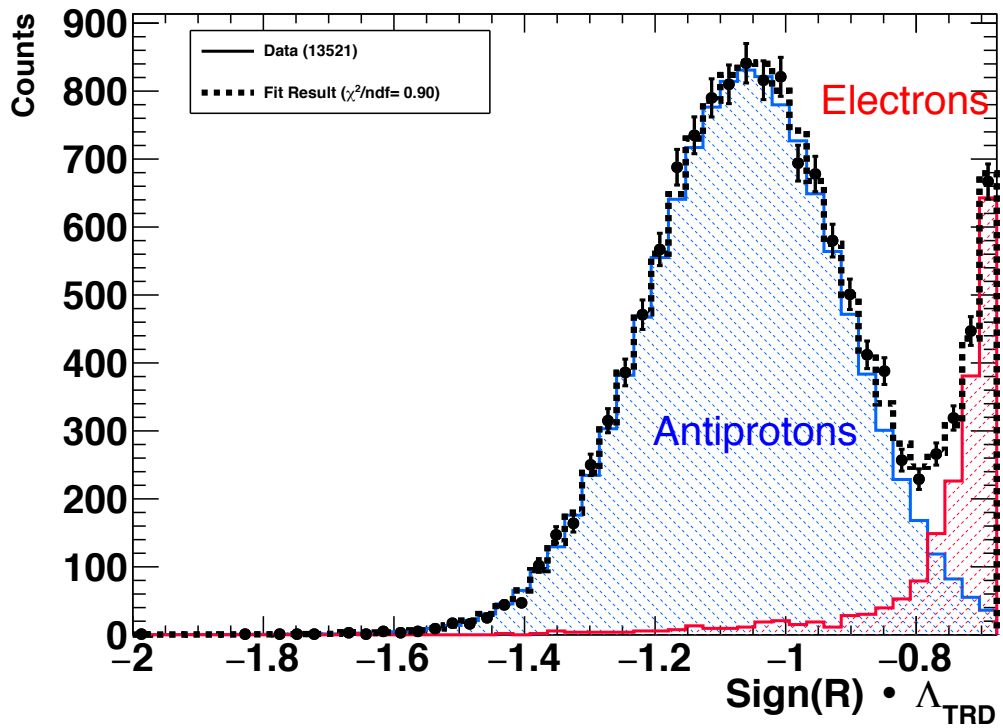


Figure 4.8: Example template fit in 10.1 to 11 GV in intermediate rigidity range

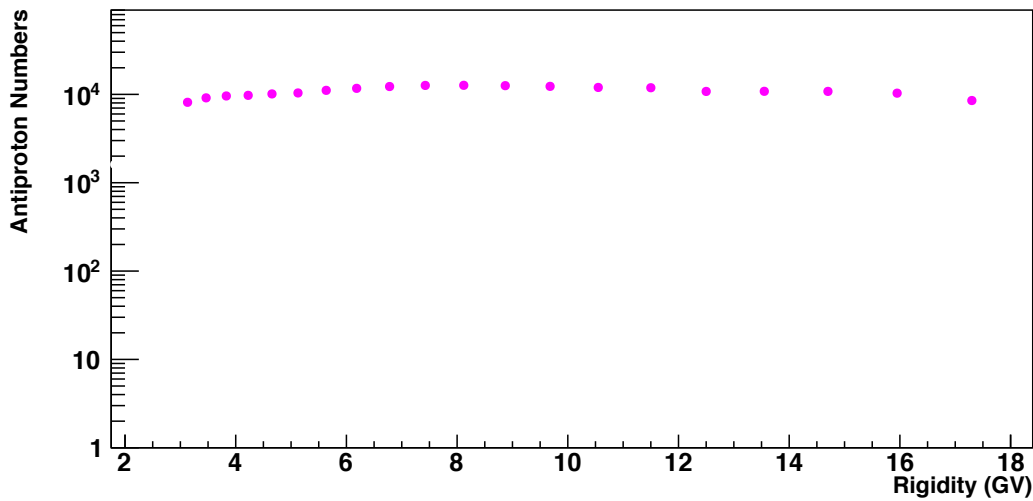


Figure 4.9: The antiproton numbers obtained from the template fit in intermediate rigidity range

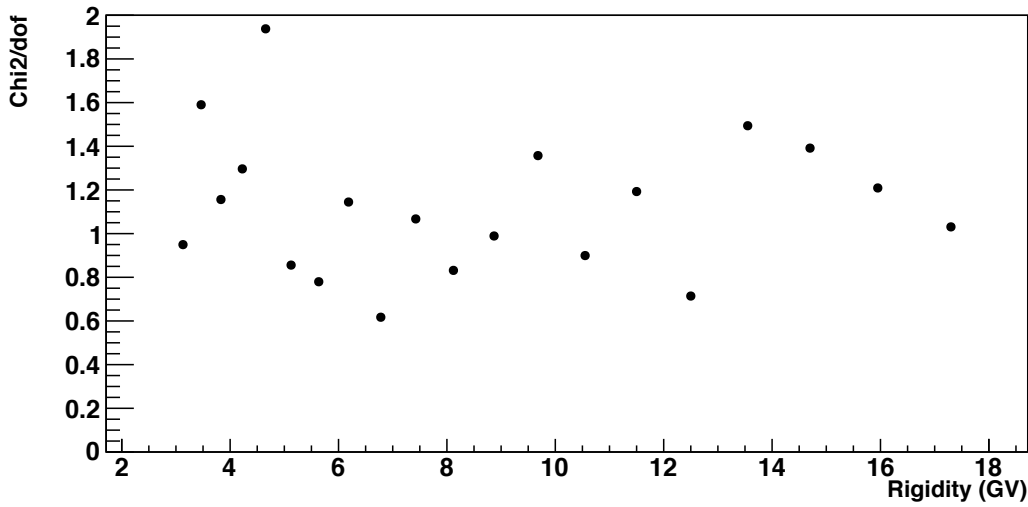


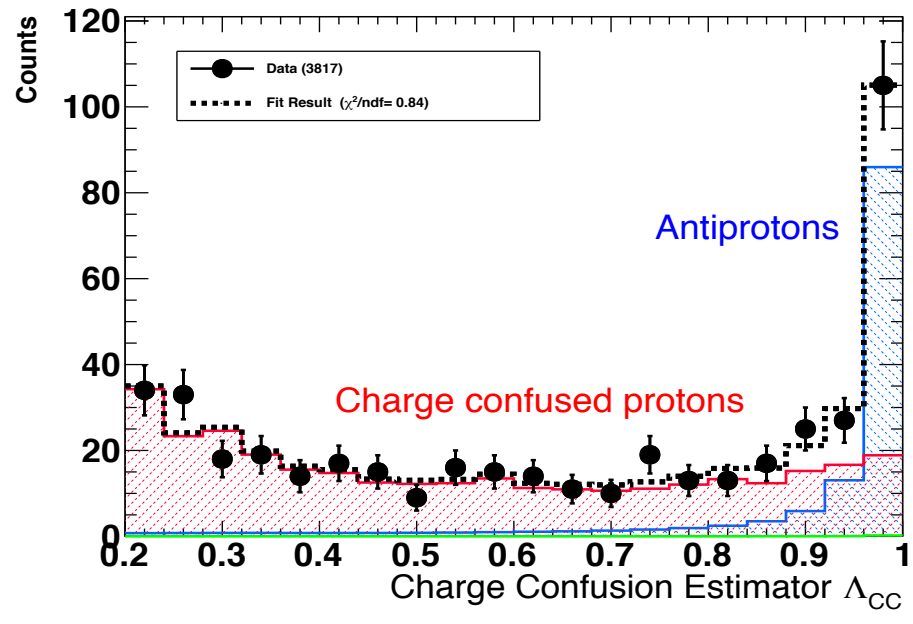
Figure 4.10: The Chi2/dof of template fit in intermediate rigidity range

825 protons. The antiproton template is taken from ISS positive rigidity data, and the electron
 826 template is taken from ISS negative rigidity data by selecting $0 < \text{ECALBDT}$, the charge
 827 confused proton is taken from proton MC simulation by selecting negative rigidity. To avoid
 828 the contamination of Helium, the $\text{TRDLikelihood}_{\text{P}/\text{He}} < 0.3$ cut is applied for the negative
 829 rigidity data before template fit.

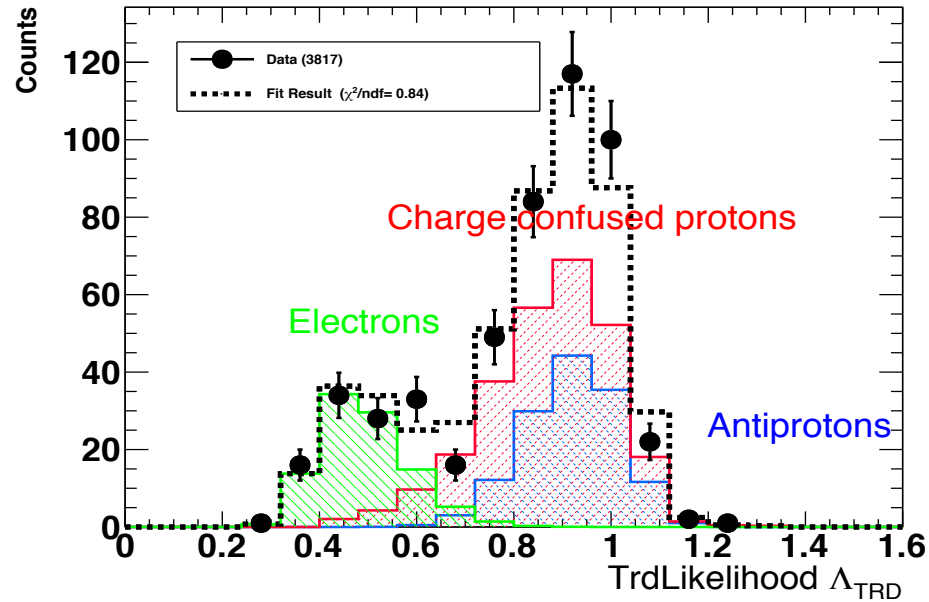
830 In figure 4.11, an example template fit in 175-211 GV is shown. To illustrate the separation,
 831 the 2D template fit is shown in two projections. In the charge confusion estimator projec-
 832 tion, the antiproton and charge confusion protons can be separated. In the TRDLikelihood
 833 projection, the antiproton and electron can be separated.

834 The antiproton got from the 2D template fit in the high rigidity range is given in figure 4.12.
 835 The correspondent Chi2/dof is given in 4.13.

836 Once the template fits in the three rigidity range is done, the antiproton numbers from 1.0
 837 to 525 GV can be obtained. In total, 481959 antiprotons are determined in this analysis.



(a)



(b)

Figure 4.11: Example template fit in 175 to 211 GV in high rigidity range. a). The charge confusion estimator projection b). The TRDLikelihood projection

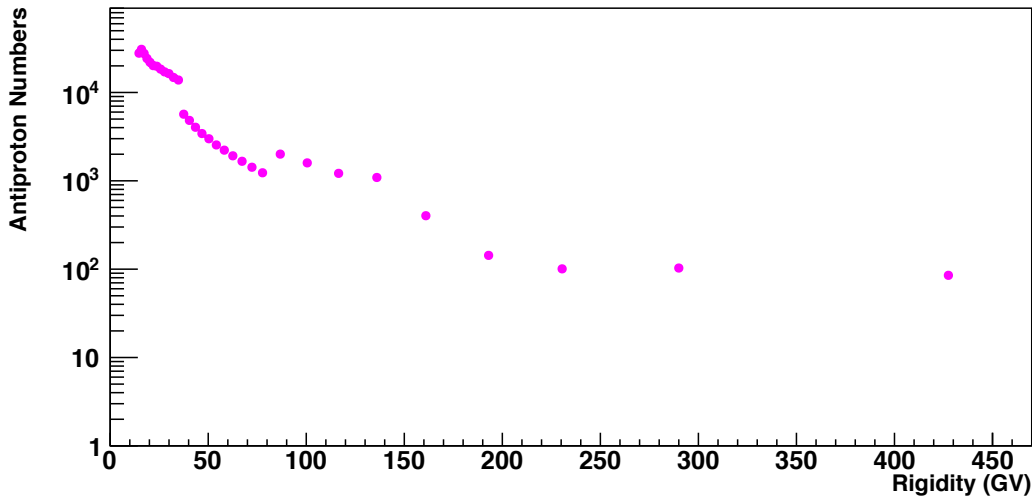


Figure 4.12: The antiproton numbers obtained from the template fit in the high rigidity range. The fluctuation is due to either merged rigidity bins width or usage of different tracker patterns.

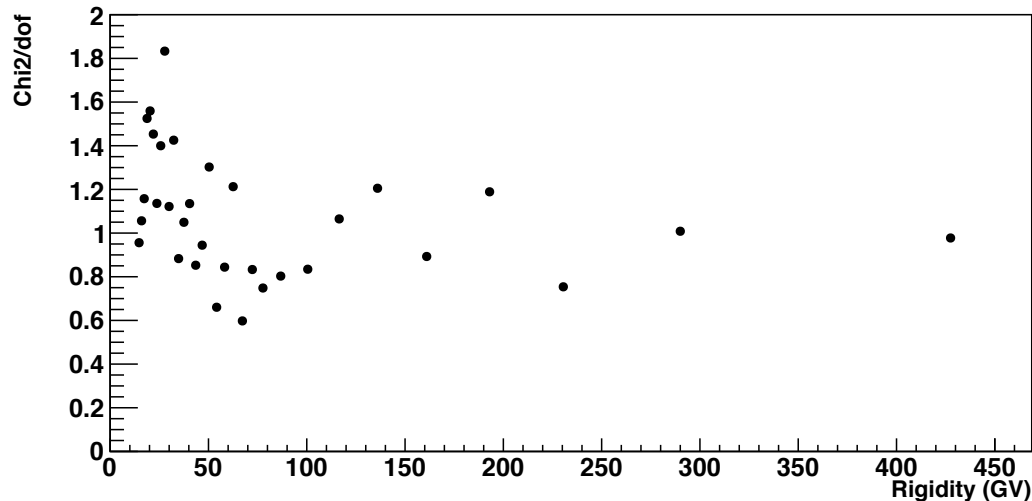


Figure 4.13: The Chi2/dof of template fit in high rigidity range

838 4.4.2. Time dependent analysis

839 For the time dependent analysis, the template fit strategy is the same as the one used in
 840 the time averaged analysis. The data is divided into every six Bartels Rotations bin. In
 841 each time bin, a template fit is performed to get the antiproton to proton ratio. Due to the
 842 limited statistics in each time bin, the rigidity bin is merged in every two original bins to

843 increase the statistics.

844 The template selections are the same as the ones used in time averaged analysis. The only
845 difference is the template fit range. To increase the statistics, the signal efficiency is increased
846 from 90% to 95% in the low rigidity range and from 90% to 98% in the intermediate rigidity
847 range.

848 A example template fit in 6.47 to 7.76 GV is given in figure 4.14. The fitted data is six
849 Bartels Rotations data taken from Jan.07.2020 to June.17.2020.

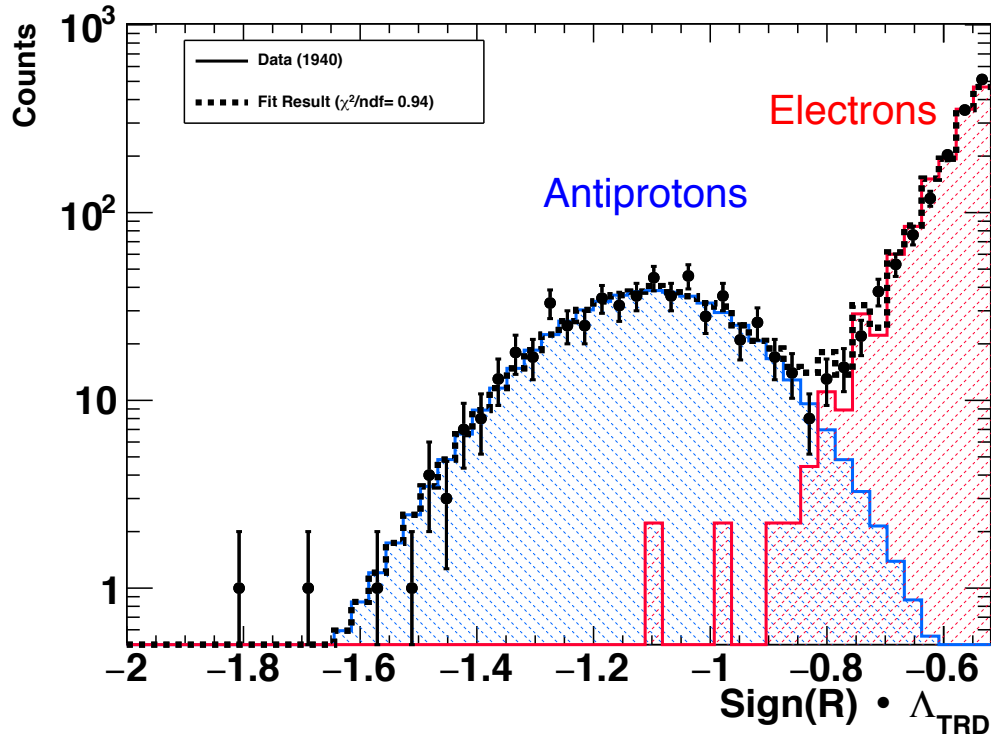


Figure 4.14: Example template fit in 6.47 to 7.76 GV with data collected Jan.07.2020 to June.17.2020.

850 The obtained antiproton numbers from the 23 six Bartel's Rotation's data is shown in figure
851 4.15. The correspondent Chi2/dof is given in figure 4.16.

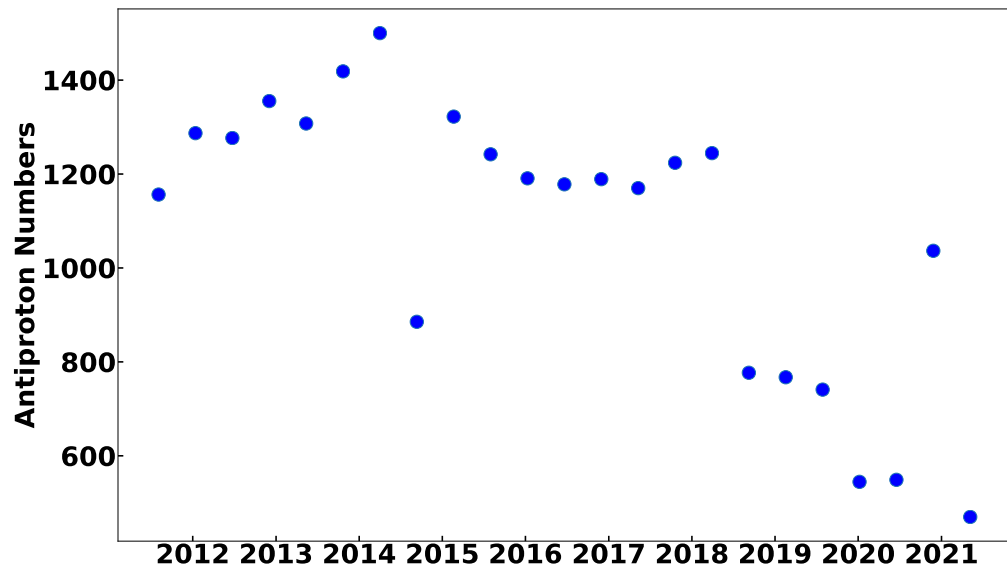


Figure 4.15: Antiproton numbers from template fit results in 6.47 to 7.76 GV with six Bartel's Rotation time resolution

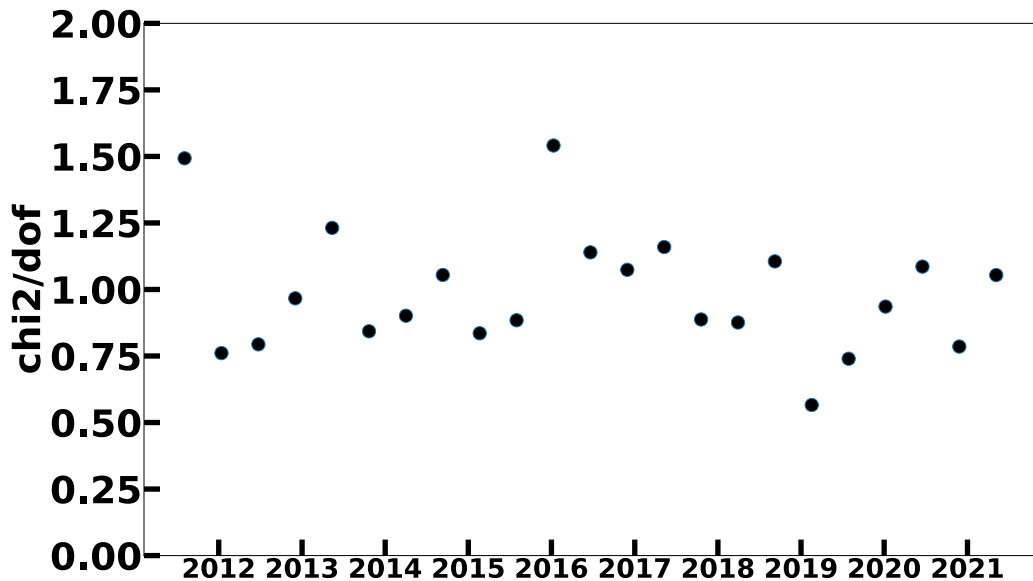


Figure 4.16: χ^2/dof of the template fits in 6.47 to 7.76 GV with six Bartel's Rotation time resolution

852 **4.5. Effective Acceptance**

853 After the event count is determined by template fit, the next important ingredient is effective
854 acceptance.

855 For a spectrometer, the counting rate of a given specie particle depends on the flux intensity
856 and the gathering factor, namely geometrical acceptance [96]. The geometrical acceptance
857 is a fixed value for a fixed apparatus, but this assumes no interaction between the traversing
858 particles and the apparatus. While for data analysis, dedicated cuts and selections should
859 be applied. Therefore, considering this, the geometrical acceptance should be multiplied by
860 the efficiencies of the cuts and selections. The product is called effective acceptance. See
861 the equation 4.4. The larger the effective acceptance is, the more events can be collected.

$$A_{eff} = A_{geo} \times \epsilon_{cut} \quad (4.4)$$

862 Calculating the acceptance directly is not easy. The more practical way is to use the MC
863 simulation method. In the AMS-02 experiment, extensive MC models with the help of
864 Geant4 are widely used. The models assume that the whole detector is located in a cube
865 with an edge length of 3.9 m. Above the top surface, a hypothetical flux source $S_{generate}$ is
866 continuously emitting particles. These artificial particles are generated from this top plane
867 and randomly go down through the whole detector.

868 According to [96], the acceptance can be calculated with two ingredients: the number of
869 triggered events $N_{triggered}$ and the number of generated events above the top plane $N_{generate}$.
870 The formula is given in equation 4.5. For the calculation of geometrical acceptance, it can
871 be achieved without applying any cuts and selections, and the triggered events can only be
872 determined by the geometry of the detectors. For the calculation of effective acceptance,
873 apart from the geometry of the detectors, the cut efficiency also reduces the number of
874 triggered events.

$$A_{eff} = \pi \cdot A \cdot \frac{N_{triggered}(R_{true})}{N_{generate}(R_{true})} \quad (4.5)$$

875 where $A = 3.9m \cdot 3.9m$.

876 The antiproton and proton effective acceptance is taken from MC. Due to the small difference
877 in passing efficiency between ISS data and MC, the effective acceptance from MC needs to be
878 corrected with the Data/MC efficiency ratio. For flux analysis, this has to be done with
879 the "Tag and Probe" method.

880 For antiproton to proton flux ratio analysis, the effective acceptance ratio is not equal
881 to one because of the differences in cross sections between antiproton and proton. The
882 effective acceptance ratio is rigidity dependent. While for the proton and antiproton effective
883 acceptances, both of them should apply a data/MC correction, and this correction can

strictly be canceled out. See equation 4.6. The way to deal with it is the same as the one used in positron/electron ratio analysis in [97]. Therefore, the effective acceptance ratio is purely determined by MC simulations.

$$\frac{A_p}{A_{\bar{p}}} = \frac{A_p^{MC}}{A_{\bar{p}}^{MC}} \cdot \frac{1 + \delta_p}{1 + \delta_{\bar{p}}} = \frac{A_p^{MC}}{A_{\bar{p}}^{MC}} \quad (4.6)$$

In figure 4.17, the antiproton to proton effective acceptance ratio is shown. In different rigidity ranges, the selections are slightly different. Therefore the effective acceptance ratios are also determined individually.

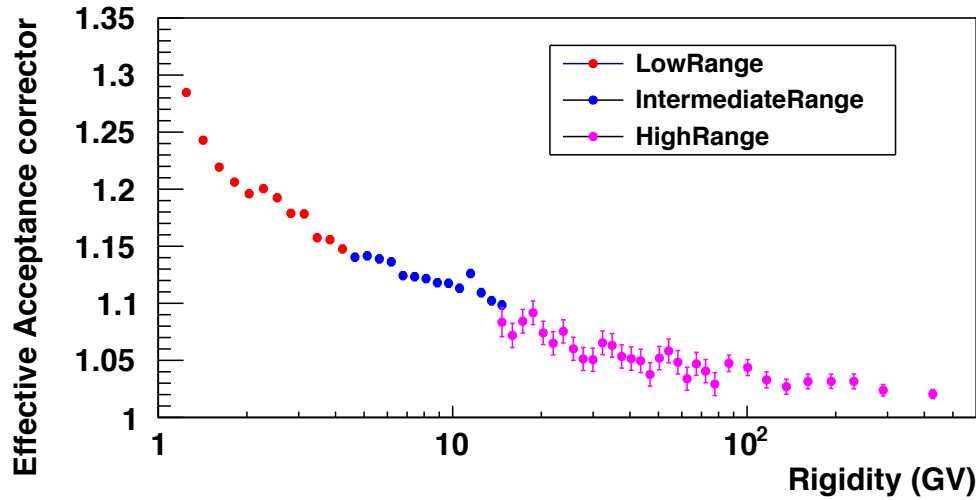


Figure 4.17: Proton to antiproton effective acceptance ratio in three rigidity ranges.

4.6. Measuring Time

To construct the flux, the next ingredient is measuring time. The measuring time is the total time that all the sub-detectors are in nominal operation and could record events. Due to the detector's operation cuts and the trigger dead time, the measuring time is lower than the exposure time, which is the total data-taking time when the experiment is running.

Because of the trigger dead time, if the event trigger rate goes up and surpasses the threshold, then not all the events can be fired and recorded. This leads to a ratio of recorded events over all events, called live time fraction. Because the amount of incoming particles depends on the ISS position in the geomagnetic field, the live time fraction is close to one in most areas but less than one in high latitude areas, see 4.18. Also, in SAA, there are plenty of low energy particles going through. Therefore, the trigger rate in this area is very high, and the live time fraction is very low correspondently. For the entire data-taking period, the

902 live time fraction is mostly above 90%. In figure 4.20, the trigger vs. particles per trigger is
903 presented. For most triggers, the number of analysis particles per trigger is around 0.11.

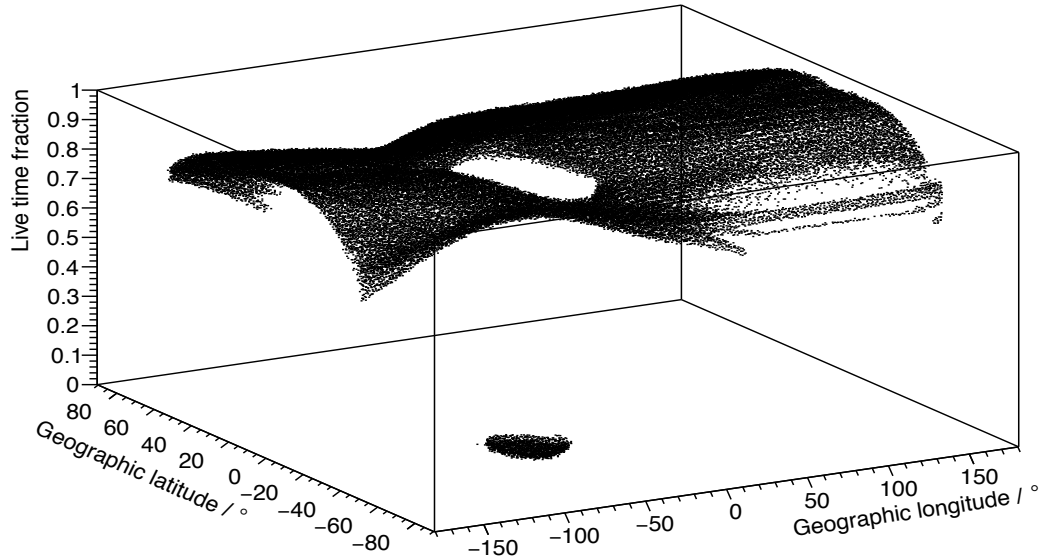


Figure 4.18: Live time fraction vs. ISS position. The live time fraction in most area is above 0.9 while in SAA is extremely low.

904 Due to the earth's magnetic field, the charged particle can be deflected before it reaches the
905 detectors at Low Earth Orbit (LEO), where the AMS-02 is located. The deflection power
906 depends on the particle's rigidity and the particle's relative location to the magnetic field
907 line.

908 The earth's magnetic field is roughly tilted at 11° with respect to the earth's rotation axis,
909 as illustrated in figure 4.21. Therefore, the lowest rigidity threshold to penetrate the earth's
910 magnetic field should be a function of the earth's location. The lowest rigidity threshold is
911 called *rigidity cutoff*.

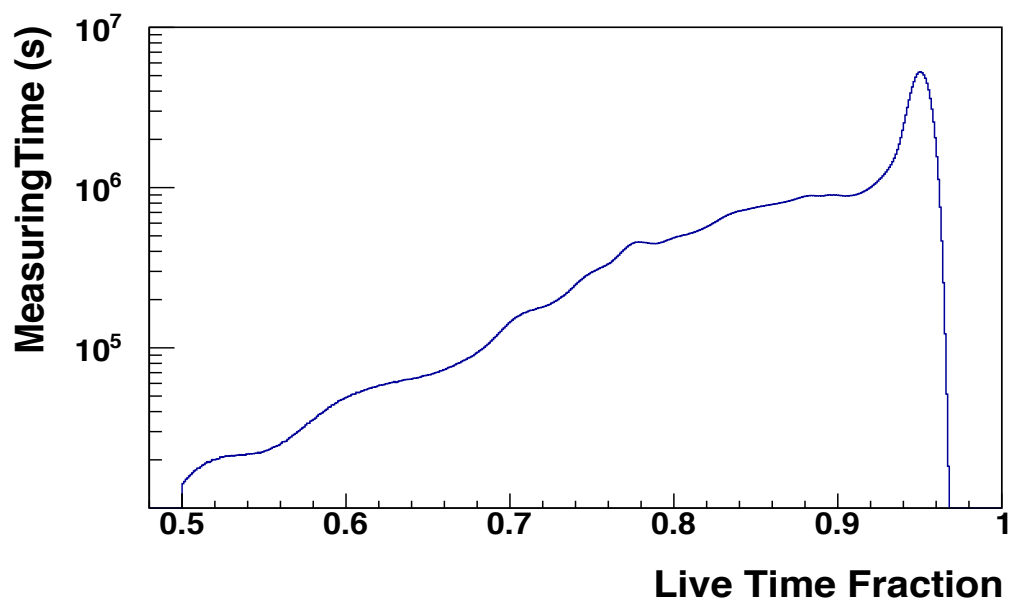


Figure 4.19: Measuring time as a function of live time fraction. In most of the measuring time, the live time fraction is above 0.9.

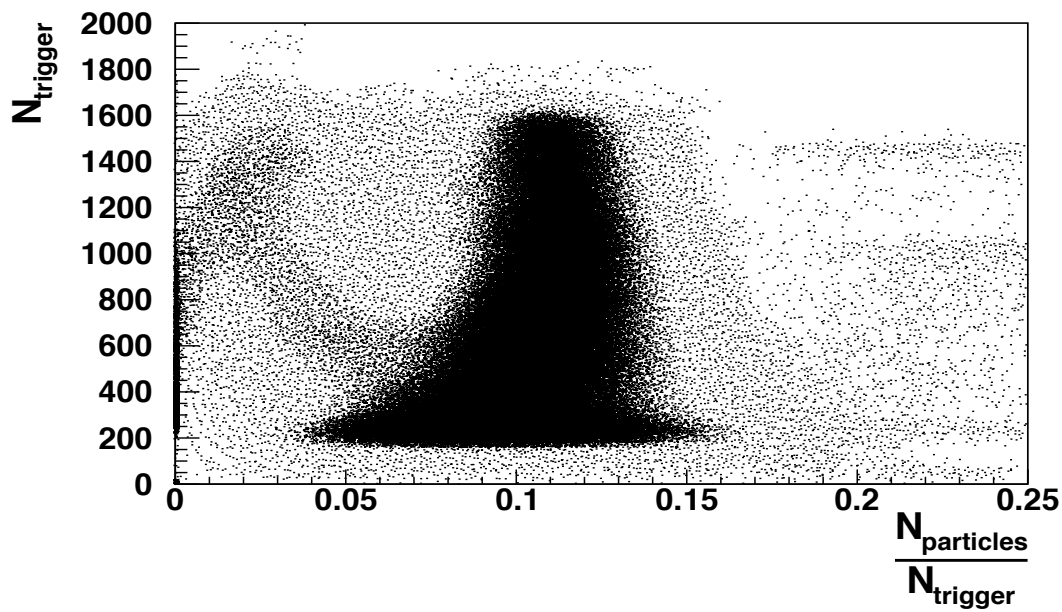


Figure 4.20: Triggers as a function of particle over trigger ratio. For most triggers, each trigger fires around 0.11 particles

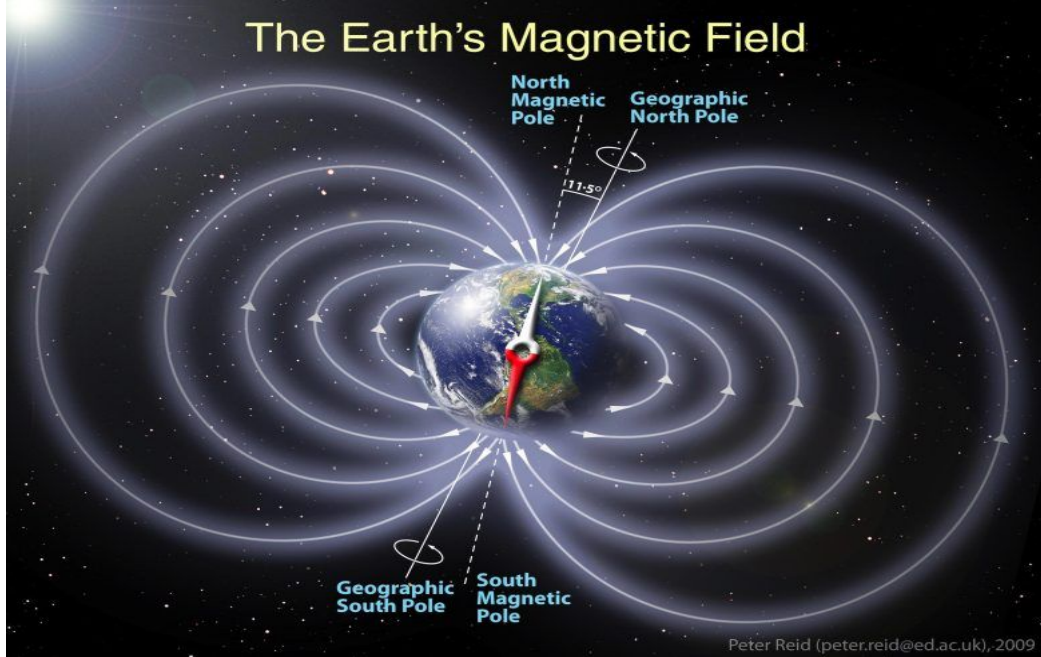


Figure 4.21: Illustration of Earth's magnetic field. Credit: Peter Reid, The University of Edinburgh

912 To calculate the rigidity cutoff, there are two methods used in AMS-02 collaboration. The
 913 first one is the Størmer cutoff, the equation 4.7 gives the way to calculate the Størmer
 914 rigidity cutoff R_c [98] :

$$R_c = \frac{M \cos^4 \lambda}{r^2 (1 + \sqrt{1 - \sin \epsilon \cdot \sin \delta \cdot \cos^3 \lambda})^2} \quad (4.7)$$

915 where M is the geomagnetic dipole moment, λ is the magnetic latitude, r is the altitude dis-
 916 tance from the dipole center, ϵ and δ are the zenith angle and azimuthal angle, respectively.

917 With the cuts and selection introduced in section 4.1, the calculated Størmer rigidity cutoff
 918 as function of ISS position is given in figure 4.22.

919 The total measuring time can be obtained by integrating the live time fraction in every
 920 second of the whole data-taking period. With the preselection about sub-detector operation
 921 quality introduced in section 4.1, the resulting measuring time used in this analysis is shown
 922 in figure 4.23. The integrated data-taking time from 20. May 2011 to 03. May 2021 is
 923 3636 days. Because of the ISS orientation, detectors operation like TRD gas refills or in the
 924 SAA, the actual measuring time is around 68% of the total data taking time. This leads to
 925 a measuring time of 2488 days.

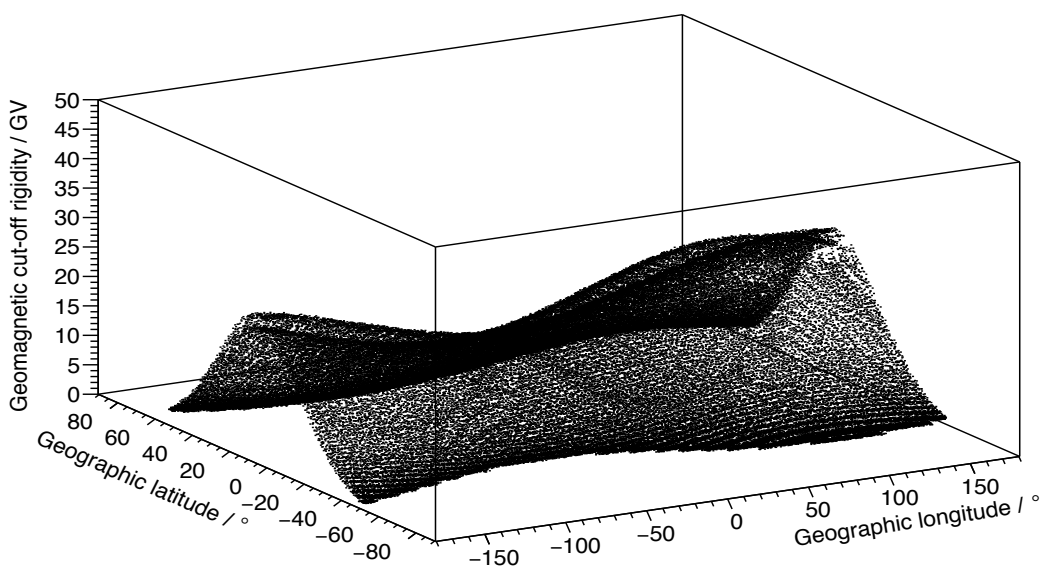


Figure 4.22: The Størmer rigidity cutoff used in this analysis as a function of ISS Position. The maximum of the cutoff is less than 30 GV.

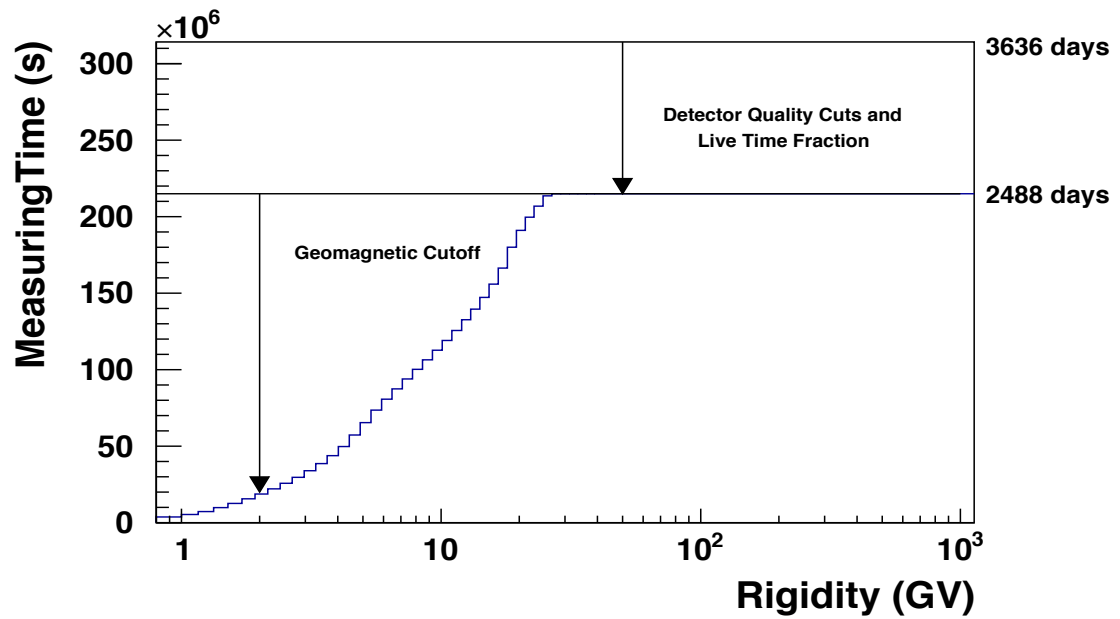


Figure 4.23: The measuring time obtained from the Størmer geomagnetic cutoff. After the quality cuts and live time fraction, the resulting total measuring time is around 2488 days.

926 Another method used in AMS-02 collaboration to calculate the rigidity cutoff is the IGRF
927 method. To calculate the particle penetrating the magnetic field, a solution is to consider
928 the backtracing particles. If all the backtracing particles from a certain position and rigidity
929 are primary particles, namely from outer space, the rigidity is the cutoff rigidity for this
930 position. The magnetic field model should be determined first in this numerical calculation
931 of backtracing particles. One model option is the International Geomagnetic Reference
932 Field (IGRF) model. Therefore, the name for calculating the rigidity cutoff is called IGRF
933 method.

934 Figure 4.24 shows the comparison between the measuring time achieved from the IGRF
935 method and the Størmer cutoff method. As shown in the figure, compared to the IGRF
936 method, using the Størmer cutoff leads to higher statistics in the low rigidity range. This is
937 important for time dependent analysis since the statistics in the fine time bin are limited.
938 Also, using the IGRF method leads to almost zero measuring time in the first one to two
939 rigidity bins. Therefore, the data could only be analyzed in higher rigidity bins. So in this
940 analysis, the Størmer rigidity cutoff is used to determine the measuring time.

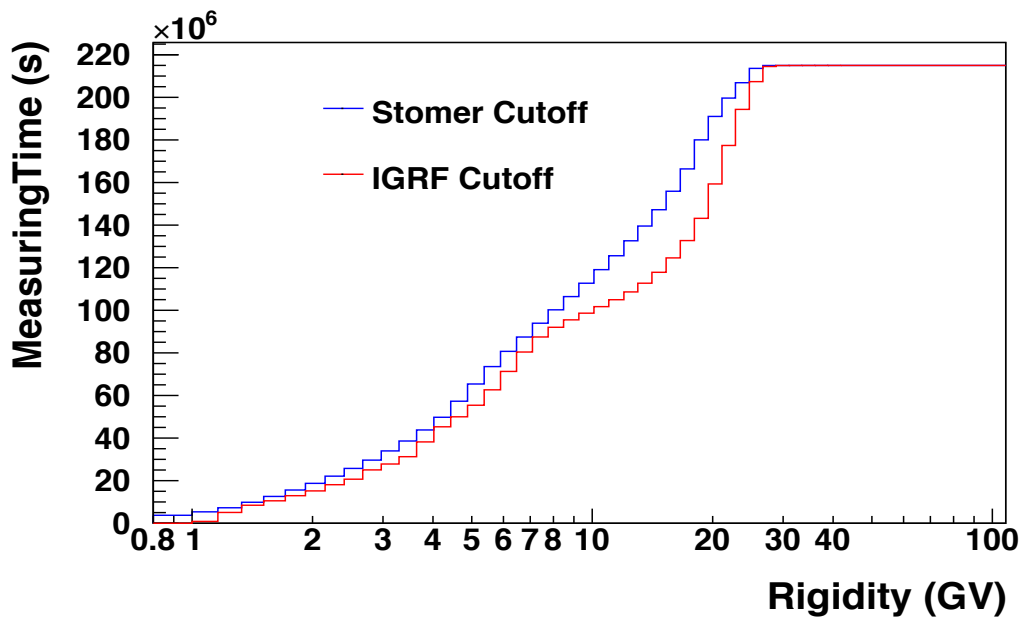


Figure 4.24: The comparison between the Størmer and IGRF cutoffs. The IGRF cutoff leads to lower measuring time

941 4.7. Trigger Efficiency

942 After the measuring time, the next ingredient to construct flux is trigger efficiency.

943 The trigger efficiency is the triggered events over the total events when the particles go

944 through the detectors. In the AMS-02 experiment, the trigger logic is based on the response
 945 of the TOF, the ACC, and the ECAL. There are three stages in AMS-02 trigger architecture:
 946 "Fast trigger", "Level 1 trigger", and "Level 3 trigger". The three stages are processed in
 947 sequence, namely the next stage is activated after the previous stage is fulfilled. Because
 948 the bandwidth is enough to transfer the data to the ground, the "Level 3 trigger" is not
 949 activated.

950 There are two kinds of "Fast trigger" [86] . The first one is using the TOF. If the FTC
 951 and FTZ trigger decisions (see definition in [89]) are fulfilled, the first kind of fast trigger
 952 is set. The second one is using the ECAL. This kind of trigger is generated by showers
 953 detected by the ECAL. The first and second fast triggers are for charged particles and
 954 photons respectively.

955 The "Layer 1 trigger" has seven kinds:

- 956 • Single charged: Has High Threshold signals (HT) in all four TOF layers, also no ACC
 957 hits.
- 958 • Fast ions: Has Super High Threshold (SHT) signals in all four TOF layers, also less
 959 than five ACC hits. (From 26 Feb 2016, the second condition changed to less than
 960 eight ACC hits to improve statistics.)
- 961 • Slow ions: Has SHT signals in all four TOF layers within 640 ns.
- 962 • Electrons: Has HT signals in all four TOF layers, also requires at least two ECAL
 963 superlayers signals in both XZ and YZ planes.
- 964 • Photons: Has an ECAL shower with less than 20 degree zenith angle in both XZ and
 965 YZ planes.
- 966 • Unbiased TOF: Has at least three out of four TOF layer HT signals. Prescaling to 1%
 967 in order to reduce the trigger rate and save bandwidth.
- 968 • Unbiased ECAL: Has signals in at least two ECAL superlayers in the X-Z or Y-Z
 969 plane. Prescaling to 0.1% to reduce the trigger rate and save bandwidth.

970 Among the seven kinds of Layer 1 triggers, the first five are called *physics trigger*. In
 971 this analysis, only the physics triggered events are used for counting the signal numbers.
 972 To construct the flux, the last two unbiased non-physics trigger are used to calculate the
 973 physics trigger efficiency.

974 Due to a technical issue in the trigger, the two unbiased triggers can be triggered at the
 975 same time, therefore the double-counting events should be corrected:

$$\frac{1}{f_{\text{both}}} = \frac{1}{f_{\text{TOF}}} + \frac{1}{f_{\text{ECAL}}} - \frac{1}{f_{\text{TOF}} \cdot f_{\text{ECAL}}} \quad (4.8)$$

976 where the $f_{TOF}=100$ is the Unbiased TOF prescaling factor and the $f_{ECAL}=1000$ is the
977 Unbiased ECAL prescaling factor. So the $f_{\text{both}} \approx 90.99$.

978 Once the prescaling factor is determined, the trigger efficiency can be calculated by com-
979 paring the number of physics trigger events and the unbiased non-physics trigger events:

$$\epsilon_{Trigger}(R) = \frac{N_{phys}(R)}{N_{phys}(R) + f_{tof} \cdot N_{tof}(R) + f_{ecal} \cdot N_{ecal}(R) + f_{tof+ecal} \cdot N_{tof+ecal}(R)} \quad (4.9)$$

980 In figure 4.25, the trigger efficiency of proton is shown as an example. For the antiproton,
981 the trigger efficiency is assumed to be the same.

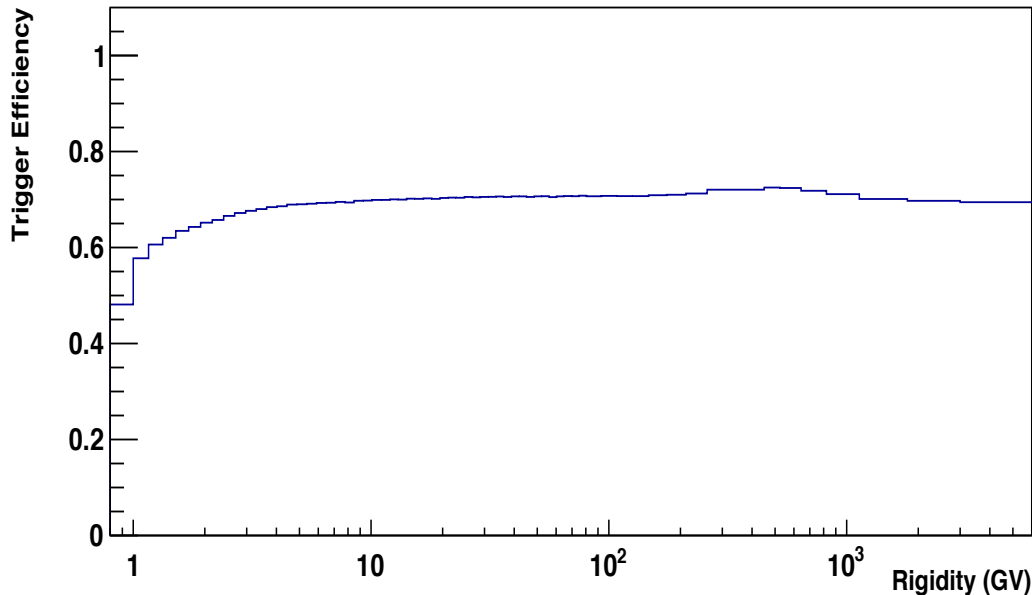


Figure 4.25: The proton trigger efficiency.

982 Since this analysis is only focused on antiproton to proton flux ratio, the trigger efficiency of
983 proton ϵ_p and antiproton $\epsilon_{\bar{p}}$ should be strictly canceled out in calculation. However, trigger
984 efficiency is still needed in the unfolding procedure in next section.

985 4.8. Unfolding

986 To calculate the flux, the number of events should be determined in true rigidity, which is the
987 rigidity at the Top Of Instrument (TOI). However, the number of events from template fit is
988 determined in reconstructed rigidity. There are some differences between these two rigidities

989 because of the limited tracker resolution. Some events may end up in other rigidity bins,
990 and this effect is called "bin to bin migration". To correct this effect, a procedure called
991 *unfolding* should be applied.

992 There are many unfolding methods to estimate this effect. In this analysis, the "Bayesian
993 unfolding" method is used. The "Bayesian unfolding" [99] is provided by the "RooUnfold"
994 package in ROOT [100], and the method is also used in AMS-02 electron and positron
995 analysis [97].

996 The unfolded count \hat{n} , namely the event count in the true rigidity, can be obtained by mul-
997 tiplying the raw event count n (the event count in reconstructed rigidity) and the unfolding
998 matrix U :

$$\hat{n} = U \cdot n \quad (4.10)$$

999 A simple correction factor by matrix inversion is the easiest way to estimate the effect, but
1000 the process is not numerically stable. Therefore the unfolding matrix U in equation 4.10 is
1001 the unfolding matrix, which is calculated in the iteration process based on migration matrix
1002 M .

1003 The migration matrix M contains the information about the "bin to bin migration" and
1004 can be taken from the MC simulation directly. The matrix is shown in a 2D histogram.
1005 The X axis is the reconstructed rigidity by the tracker, and the Y axis is the true generated
1006 rigidity simulated in the MC. In this analysis, the signals are determined with different
1007 selections for different rigidity ranges. Also, for the different tracker patterns, the migration
1008 matrices are different due to the different tracker pattern resolutions. In figure 4.26, the
1009 migration matrix of full span in high rigidity range is given as an example, which is taken
1010 from proton MC simulation. The histogram is normalized to unity for illustration. From
1011 the figure, the diagonal elements of the matrix are the events whose true rigidity matches
1012 the reconstructed rigidity, which is the dominant part of the total events. With the rigidity
1013 going up, the bin contents of non-diagonal elements are going up. This is due to the tracker
1014 resolution becoming worse in higher rigidity.

1015 As introduced in the section 4.6, the collected data have applied the rigidity cutoff. This
1016 cutoff effect is not simulated in the MC simulation process, so it must be fixed before we
1017 use the migration matrix. To consider this, the shape of measuring time is used as a weight
1018 for the events under the rigidity cutoff.

1019 In this analysis, the focus is the antiproton to proton ratio. Therefore, the unfolding process
1020 has to be done for antiproton raw numbers and proton raw numbers respectively. The
1021 antiproton raw numbers are taken from template fit results, and the proton raw numbers
1022 are the event numbers after the cuts and selections shown before. In figure 4.27, the residual
1023 of raw counts and unfolded counts in the high rigidity range is given. The overall correction
1024 effect is less than 10% in the unfolded ratio.

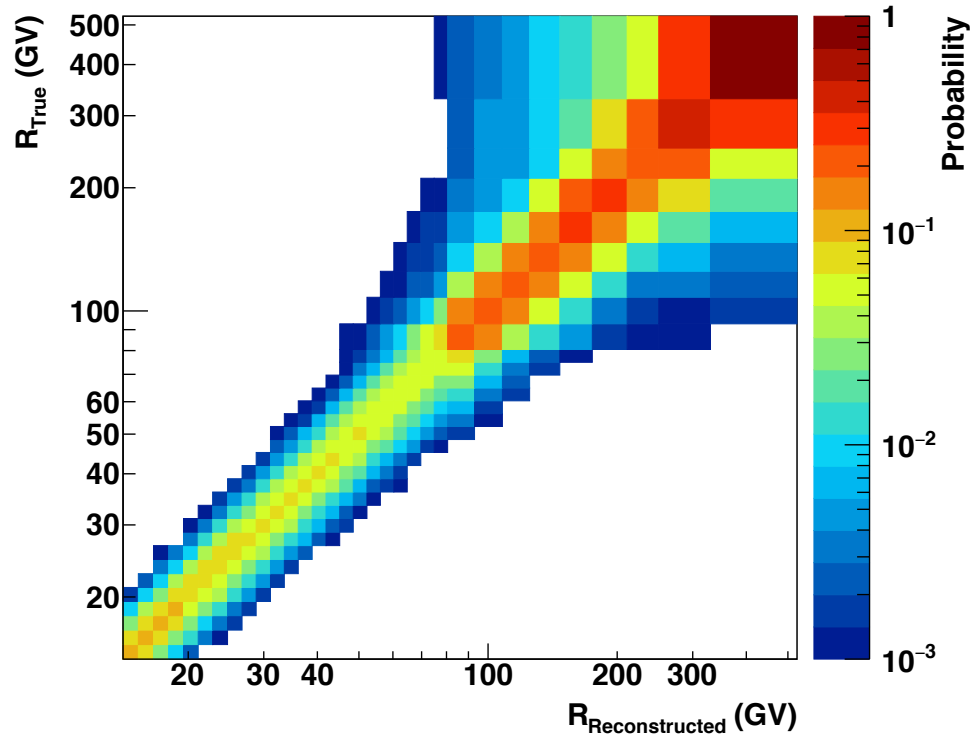


Figure 4.26: The migration matrix for full span in high rigidity range. The X axis is the reconstructed rigidity from the Tracker, the Y axis is the true rigidity from the generated momentum in MC.

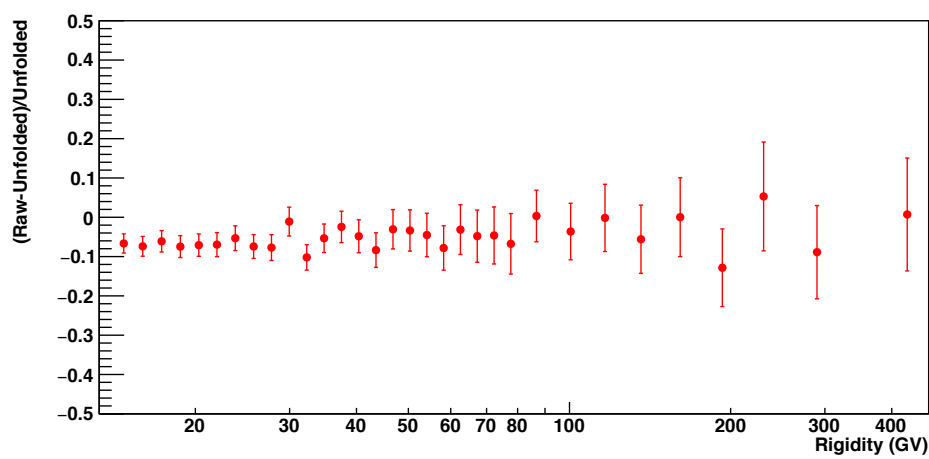


Figure 4.27: The residual over unfolded number for full span in high rigidity range

1025 **4.9. Antiproton To Proton Flux Ratio Calculation**

1026 In this section, the calculation of the antiproton to proton flux ratio is given.

1027 This thesis focuses on the antiproton to proton flux ratio. Therefore the dedicated formula
 1028 for antiproton to proton flux ratio should also be discussed in advance based on flux calcu-
 1029 lation equation 4.1. From previous sections in this chapter, all the ingredients have been
 1030 shown already, so the antiproton to proton flux ratio can be calculated.

$$\begin{aligned}\Phi_{\bar{p}}(|R|) &= \frac{N_{\bar{p}}(|R|)}{\Delta R_{\bar{p}} \cdot T_{\bar{p}}(|R|) \cdot A_{\bar{p}}(|R|) \cdot \epsilon_{\bar{p}}(|R|)} \\ \Phi_p(|R|) &= \frac{N_p(|R|)}{\Delta R_p \cdot T_p(|R|) \cdot A_p(|R|) \cdot \epsilon_p(|R|)}\end{aligned}\quad (4.11)$$

1031 By definition, the antiproton to proton flux ratio is the antiproton flux divided by the proton
 1032 flux. In this process, some terms can be strictly canceled out, like the procedure of AMS-02
 1033 positron to electron flux ratio analysis in [97]. Therefore, the overall calculation can be
 1034 simplified:

$$\begin{aligned}\frac{\Phi_{\bar{p}}(|R|)}{\Phi_p(|R|)} &= \frac{N_{\bar{p}}(|R|) \cdot \Delta R_p \cdot T_p(|R|) \cdot A_p(|R|) \cdot \epsilon_p(|R|)}{N_p(|R|) \cdot \Delta R_{\bar{p}} \cdot T_{\bar{p}}(|R|) \cdot A_{\bar{p}}(|R|) \cdot \epsilon_{\bar{p}}(|R|)} \\ &= \frac{N_{\bar{p}}(|R|)}{N_p(|R|)} \frac{A_p(|R|)}{A_{\bar{p}}(|R|)} \\ &= \frac{N_{\bar{p}}(|R|)}{N_p(|R|)} \frac{A_p^{MC}(|R|)}{A_{\bar{p}}^{MC}(|R|)} \frac{1 + \delta_p(|R|)}{1 + \delta_{\bar{p}}(|R|)} \\ &= \frac{N_{\bar{p}}(|R|)}{N_p(|R|)} \frac{A_p^{MC}(|R|)}{A_{\bar{p}}^{MC}(|R|)}\end{aligned}\quad (4.12)$$

1035 From the dedicated equation 4.12 for antiproton to proton flux ratio, obviously some terms
 1036 are canceled out like measuring time, trigger efficiency, rigidity bin width, and the data/MC
 1037 corrections of effective acceptance. This gives many conveniences for calculation. Although
 1038 the measuring time and trigger efficiency is canceled out in the ratio calculation, they are
 1039 still used in the unfolding process.

1040 The formula for the time dependent antiproton to proton flux ratio is the same. The only
 1041 difference is the number of event is taken from individual template fit in every six Bartels
 1042 Rotations bins.

1043 4.10. Systematic Uncertainty

1044 In this section, systematic uncertainty is discussed. Due to different template fit methods in
1045 three different rigidity ranges. The systematic uncertainty is discussed individually in three
1046 rigidity ranges.

1047 The antiproton to proton flux ratio is calculated in equation 4.12. There are two components
1048 in this equation: Number of events N and effective acceptance A. Therefore, the sources of
1049 systematic uncertainty should also be considered from these two variables.

1050 The first source of systematic uncertainty is effective acceptance. Since the effective accep-
1051 tance data/MC correction is canceled out, so it is completely decided by the MC simulation.
1052 Due to the asymmetry of the interaction cross sections, the antiproton and proton effective
1053 acceptances impact the flux ratio. Therefore, two dedicated MCs are generated for antipro-
1054 ton and proton respectively to estimate the asymmetry of the interaction cross sections. In
1055 these two MCs, the interaction cross sections are varied with $\pm 10\%$ change. This transfers
1056 to systematic uncertainty from effective acceptance. In figure 4.28, the obtained systematic
1057 error is shown.

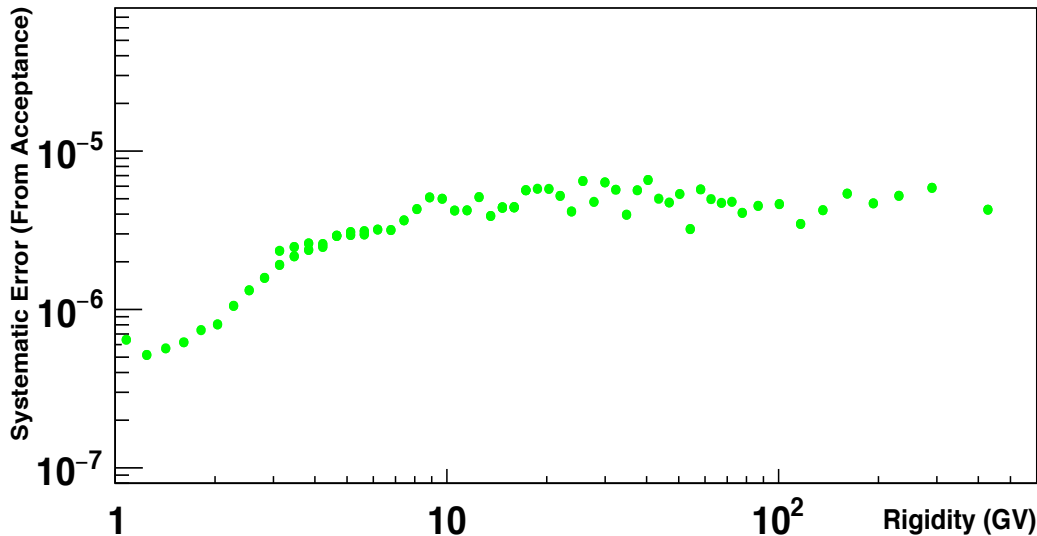


Figure 4.28: The systematic error from acceptance

1058 The second source of systematic uncertainty is the event number. In different rigidity ranges,
1059 the antiproton signal number is determined with diverse backgrounds and different template
1060 fit methods. Therefore, it has to be calculated individually in different rigidity ranges.

1061 In the low rigidity range, the antiproton signal is derived from a 2D template fit in 1/TOF-
1062 Beta and TRDLikelihood. A variation of the template fit range is used to estimate the

1063 template fit result. As introduced in section 4.4, the official result is chosen from the tem-
 1064 plate fit range in 90% signal efficiency. To estimate the systematic uncertainty, the template
 1065 fit is performed 342 times with signal efficiency 40% to 95%. For the first five points, the
 1066 signal efficiency range is from 65% due to the low statistics. Then the RMS of the result
 1067 distribution is chosen as the systematic error in each rigidity bin.

1068 In the intermediate rigidity range, the same logic to calculate systematic uncertainty is
 1069 used, but the difference is the template fit in intermediate rigidity is 1D template fit in
 1070 TRDLikelihood. So in this range, the template fit is performed from 60% to 100% signal
 1071 efficiency range.

1072 In figure 4.29, an example of template fit results from different signal efficiency is shown.
 1073 The rigidity bin is 2.15 to 2.4 GV, and the RMS of the results is used as the systematic
 1074 error in this bin.

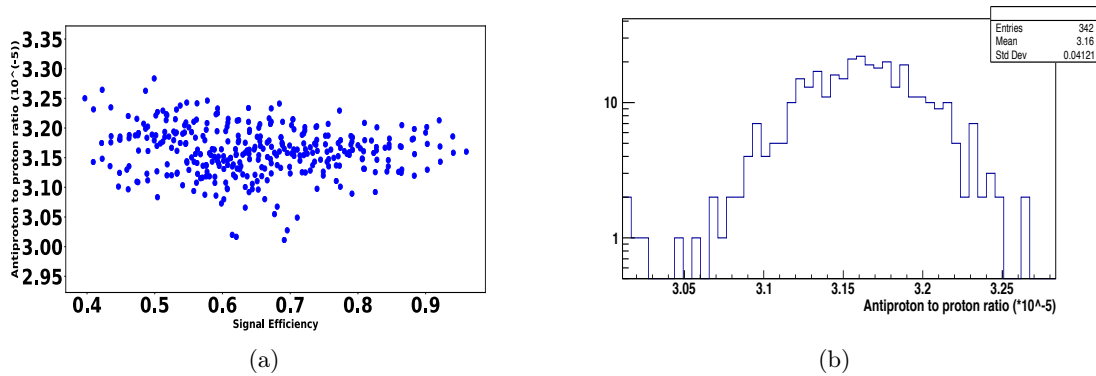


Figure 4.29: The template fit result in 2.15 to 2.4 GV with signal efficiency from 40%. a). The template fit result distribution as a function of signal efficiency. b). The template fit result histogram. The RMS of the histogram is used as the systematic error.

1075 In figure 4.30, the systematic uncertainty from the template fit range is shown. The absolute
 1076 error is relatively stable at around 10^{-6} .

1077 In the high rigidity range, the charge confused proton background rises dramatically with
 1078 rigidity going up. The template of charge confused proton, which is taken from proton MC,
 1079 becomes the primary source of systematic error, replacing the template fit range.

1080 To estimate the charge confusion systematic error, the charge confusion level (CC Level)
 1081 between MC and ISS data is used. The CC Level is defined as the charge confused proton
 1082 number over the sum of charge confused proton number and charge correct proton number.
 1083 In figure 4.31, the MC/data CC Level ratio is shown. The uncertainty band is derived
 1084 with 68% C.L. and used as the variation of the CC Level, which transfers to charge confused
 1085 proton number. Then the template fit in the high rigidity range is redone with a fixed charge
 1086 confused proton number with the variation. This leads to antiproton numbers uncertainty

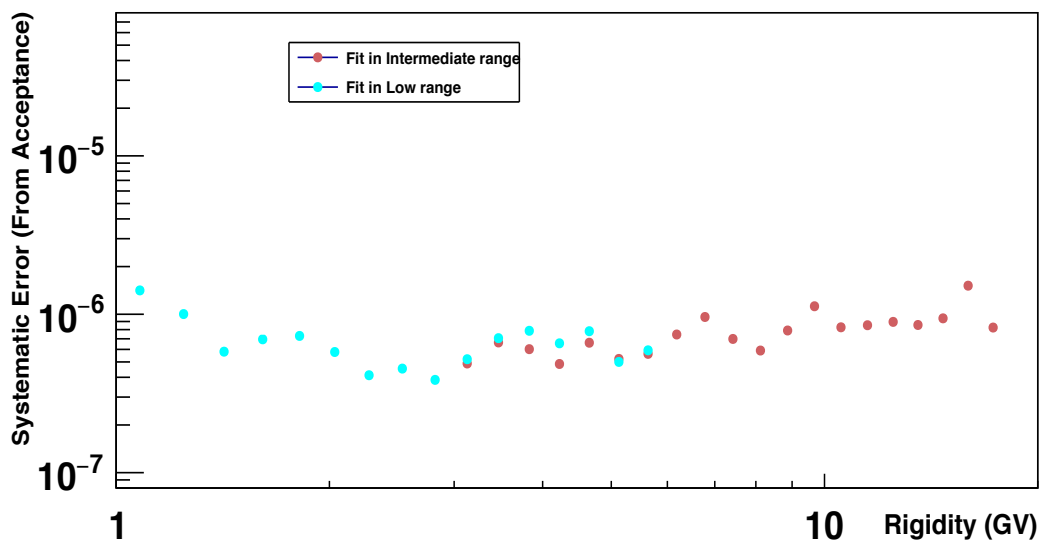


Figure 4.30: The systematic error from template fit range

¹⁰⁸⁷ due to charge confusion.

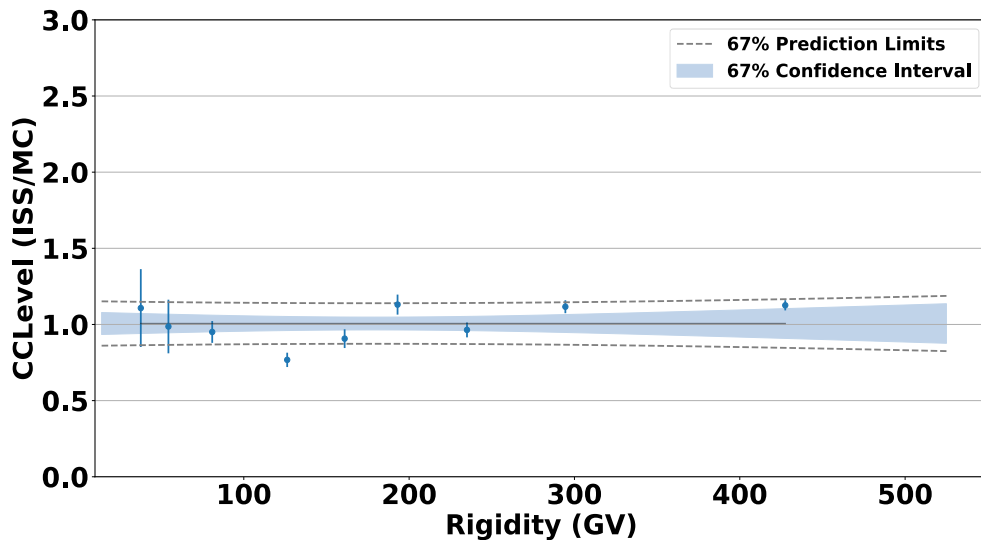


Figure 4.31: Data/MC charge confusion level ratio.

¹⁰⁸⁸ In figure 4.32 the systematic error due to charge confusion is shown.

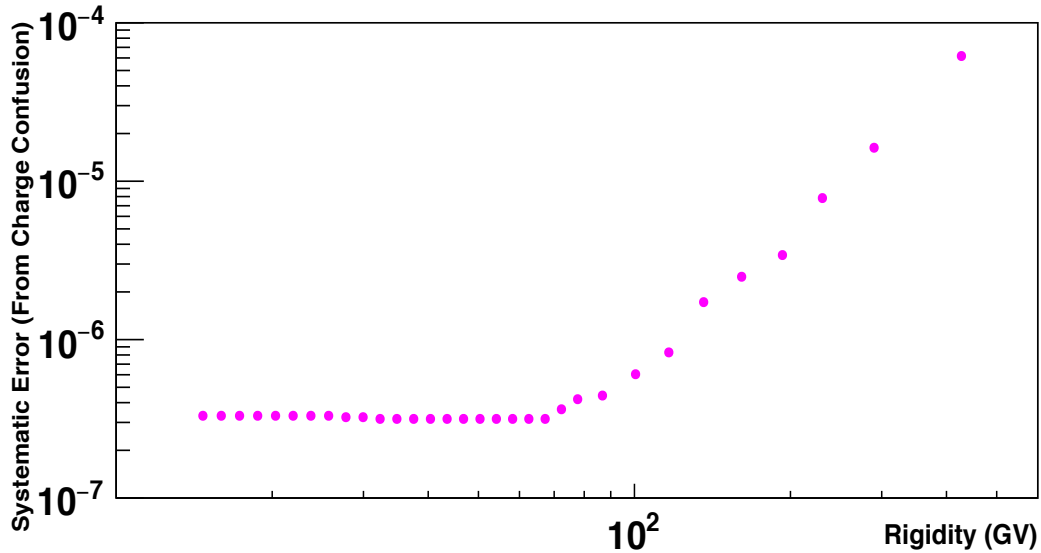


Figure 4.32: The systematic error from charge confusion

1089 The different systematic errors are added quadratically to arrive at the total systematic
 1090 error. In figure 4.33, the total systematic error is presented.

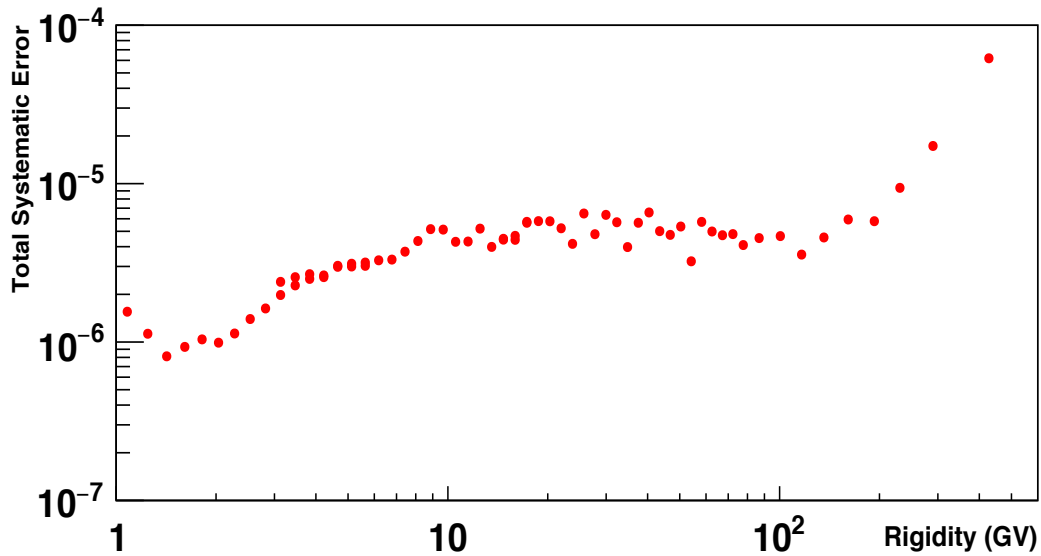


Figure 4.33: The total systematic error

1091 The statistical error is directly taken from template fit in different rigidity ranges. The total
 1092 error of the result is calculated by the square root of the sum of squares of statistical error
 1093 and systematic error.

1094 For the time dependent analysis, the same calculation way is used. Since the time depen-
1095 dent analysis is only performed below 20 GV. Therefore, only the result in the low and
1096 intermediate range is considered.

1097 In figure 4.34, the systematic error in 1.92 to 2.4 GV in six Bartels Rotation time bin is
1098 shown as an example.

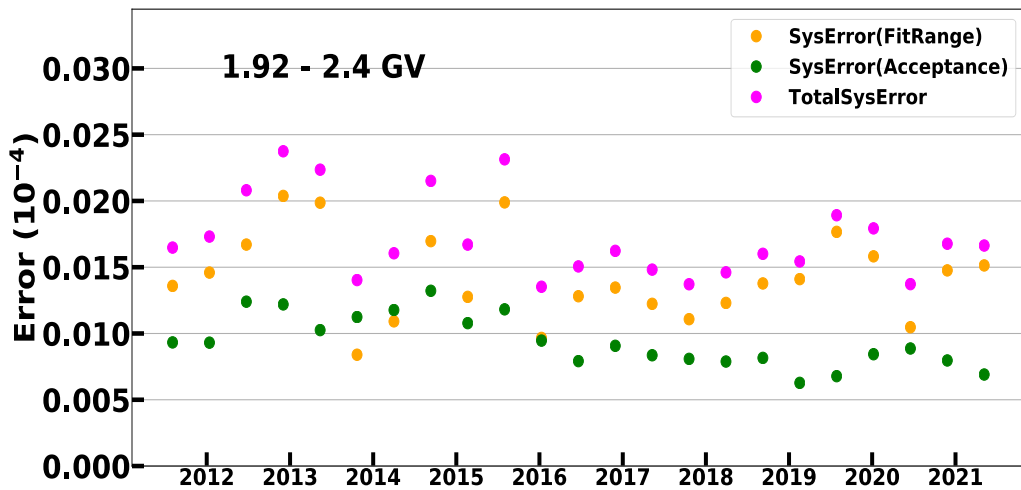


Figure 4.34: Systematic error of the antiproton to proton flux ratio in 1.92 to 2.4 GV in six Bartels Rotation time bin

BIBLIOGRAPHY

- [1] NobelPrize.org (Nobel Media AB). Victor F. Hess - Facts, 2022. URL: <https://www.nobelprize.org/prizes/physics/1936/hess/facts>.

[2] NobelPrize.org (Nobel Media AB). Carl D. Anderson - Facts, 2022. URL: <https://www.nobelprize.org/prizes/physics/1936/anderson/facts>.

[3] NobelPrize.org (Nobel Media AB). The Nobel Prize in Physics 1959, 2022. URL: <https://www.nobelprize.org/prizes/physics/1959/summary>.

[4] O. Adriani et al. Measurement of the flux of primary cosmic ray antiprotons with energies of 60-MeV to 350-GeV in the PAMELA experiment. *Pisma Zh. Eksp. Teor. Fiz.*, 96:693–699, 2012. DOI: [10.1134/S002136401222002X](https://doi.org/10.1134/S002136401222002X).

[5] Kenneth Greisen. End to the Cosmic-Ray Spectrum? *Phys. Rev. Lett.*, 16:748–750, Apr 1966. DOI: [10.1103/PhysRevLett.16.748](https://doi.org/10.1103/PhysRevLett.16.748).

[6] G T Zatsepin and V A Kuz'min. Upper Limit of the Spectrum of Cosmic Rays. *Soviet Journal of Experimental and Theoretical Physics Letters*, 4:78, Aug 1966. URL: <https://www.osti.gov/biblio/4515382>.

[7] Dinu Al. Detection of a Cosmic Ray with Measured Energy Well beyond the Expected Spectral Cutoff due to Cosmic Microwave Radiation. *Astrophysical Journal*, 441:144, Mar 1995. DOI: [10.1086/175344](https://doi.org/10.1086/175344).

[8] R. Abbasi et al. Indications of Intermediate-Scale Anisotropy of Cosmic Rays with Energy Greater than 57 EeV In the Northern sky measured with the surface detector of the telescope array experiment. *The Astrophysical Journal*, 790(2):L21, Jul 2014. DOI: [10.1088/2041-8205/790/2/l21](https://doi.org/10.1088/2041-8205/790/2/l21).

[9] Alicia Lopez Oramas. Multi-year Campaign of the Gamma-Ray Binary LS I +61° 303 and Search for VHE Emission from Gamma-Ray Binary Candidates with the MAGIC Telescopes. PhD thesis, Universitat Autonoma de Barcelona, Apr 2015. DOI: [10.13140/RG.2.1.4140.4969](https://doi.org/10.13140/RG.2.1.4140.4969).

[10] R. L. Workman and Others (Particle Data Group). Review of Particle Physics. *PTEP*, 2022:p.083C01, 2022. DOI: [10.1093/ptep/ptac097](https://doi.org/10.1093/ptep/ptac097).

[11] Alessandra Pacini. Cosmic rays: Bringing messages from the sky to the Earth's surface. *Revista Brasileira de Ensino de Fisica*, 39, Jan 2017. DOI: [10.1590/1806-9126-RBEF-2016-0168](https://doi.org/10.1590/1806-9126-RBEF-2016-0168).

[12] W. Baade and F. Zwicky. Cosmic Rays from Super-novae. *Proceedings of the National Academy of Sciences of the United States of America*, 20(5):259–263, 1934. URL: [https://doi.org/10.1073/pnas.20\(5\).259](https://doi.org/10.1073/pnas.20(5).259).

- 1188 <http://www.jstor.org/stable/86841>.
- 1189 [13] Massimo Turatto. *Classification of Supernovae*, pages 21–36. Springer Berlin Heidelberg, Berlin, Heidelberg, 2003. DOI: [10.1007/3-540-45863-8_3](https://doi.org/10.1007/3-540-45863-8_3).
- 1190
1191 [14] Stephen P. Reynolds. Supernova Remnants at High Energy. *Annual Review of Astronomy and Astrophysics*, 46(1):89–126, 2008. DOI: [10.1146/annurev.astro.46.060407.145237](https://doi.org/10.1146/annurev.astro.46.060407.145237).
- 1192
1193
1194 [15] Malcolm S. Longair. High Energy Astrophysics. UK: Cambridge University Press, 2011. URL: <https://ui.adsabs.harvard.edu/abs/2011hea..book.....L>.
- 1195
1196 [16] ENRICO Fermi. On the Origin of the Cosmic Radiation. *Phys. Rev.*, 75:1169–1174, Apr 1949. DOI: [10.1103/PhysRev.75.1169](https://doi.org/10.1103/PhysRev.75.1169).
- 1197
1198 [17] T. Gold, F. G. Smith, and A. W. Wolfendale. Pulsars and the Origin of Cosmic Rays and Discussion. *Philosophical Transactions of the Royal Society of London. Series A, Mathematical and Physical Sciences*, 277(1270):453–461, 1975. URL: <http://www.jstor.org/stable/74493>.
- 1199
1200
1201
1202 [18] Bednarek, W. and Bartosik, M. Cosmic rays from Galactic pulsars. *Astronomy & Astrophysics*, 423(2):405–413, 2004. DOI: [10.1051/0004-6361:20047005](https://doi.org/10.1051/0004-6361:20047005).
- 1203
1204 [19] J Arons. Pulsar wind nebulae as cosmic pevatrons: A current sheet’s tale. *Space Sci Rev*, 173:341–367, 2012. DOI: [10.1007/s11214-012-9885-1](https://doi.org/10.1007/s11214-012-9885-1).
- 1205
1206 [20] A. R. Bell. Cosmic ray acceleration in pulsar-driven supernova remnants. *Monthly Notices of the Royal Astronomical Society*, 257(3):493–500, Aug 1992. DOI: [10.1093/mnras/257.3.493](https://doi.org/10.1093/mnras/257.3.493).
- 1207
1208
1209 [21] Dan Hooper, Pasquale Blasi, and Pasquale Dario Serpico. Pulsars as the sources of high energy cosmic ray positrons. *Journal of Cosmology and Astroparticle Physics*, 2009(01):025, Jan 2009. DOI: [10.1088/1475-7516/2009/01/025](https://doi.org/10.1088/1475-7516/2009/01/025).
- 1210
1211
1212 [22] R. Cowsik. Positrons and Antiprotons in Galactic Cosmic Rays. *Annual Review of Nuclear and Particle Science*, 66(1):297–319, 2016. DOI: [10.1146/annurev-nucl-102115-044851](https://doi.org/10.1146/annurev-nucl-102115-044851).
- 1213
1214
1215 [23] Jan Heisig. Cosmic-ray antiprotons in the ams-02 era: A sensitive probe of dark matter. *Modern Physics Letters A*, 36(05):2130003, 2021. DOI: [10.1142/S0217732321300032](https://doi.org/10.1142/S0217732321300032).
- 1216
1217 [24] Martin Wolfgang Winkler. Cosmic ray antiprotons at high energies. *Journal of Cosmology and Astroparticle Physics*, 2017(02):048–048, Feb 2017. DOI: [10.1088/1475-7516/2017/02/048](https://doi.org/10.1088/1475-7516/2017/02/048).
- 1218
1219

- 1220 [25] Rolf Kappl and Martin Wolfgang Winkler. The cosmic ray antiproton background
 1221 for AMS-02. *Journal of Cosmology and Astroparticle Physics*, 2014(09):051–051, Sep
 1222 2014. DOI: [10.1088/1475-7516/2014/09/051](https://doi.org/10.1088/1475-7516/2014/09/051).
- 1223 [26] Andrew W. Strong, Igor V. Moskalenko, and Vladimir S. Ptuskin. Cosmic-Ray Propa-
 1224 gation and Interactions in the Galaxy. *Annual Review of Nuclear and Particle Science*,
 1225 57(1):285–327, 2007. DOI: [10.1146/annurev.nucl.57.090506.123011](https://doi.org/10.1146/annurev.nucl.57.090506.123011).
- 1226 [27] Igor V. Moskalenko. Galprop: modeling cosmic ray propagation and associated inter-
 1227 stellar emissions, 2011. DOI: [10.48550/ARXIV.1105.4921](https://arxiv.org/abs/1105.4921).
- 1228 [28] David Maurin. usine: Semi-analytical models for Galactic cosmic-ray prop-
 1229 agation. *Computer Physics Communications*, 247:106942, 2020. DOI:
 1230 [10.1016/j.cpc.2019.106942](https://doi.org/10.1016/j.cpc.2019.106942).
- 1231 [29] Carmelo Evoli, Daniele Gaggero, Andrea Vittino, Giuseppe Di Bernardo, Mattia Di
 1232 Mauro, Arianna Ligorini, Piero Ullio, and Dario Grasso. Cosmic-ray propagation
 1233 with DRAGON2: I. numerical solver and astrophysical ingredients. *Journal of Cos-
 1234 mology and Astroparticle Physics*, 2017(02):015–015, Feb 2017. DOI: [10.1088/1475-
 1235 7516/2017/02/015](https://doi.org/10.1088/1475-7516/2017/02/015).
- 1236 [30] V. S. Ptuskin, O. N. Strelnikova, and L. G. Sveshnikova. On leaky-box
 1237 approximation to GALPROP. *Astropart. Phys.*, 31:284–289, 2009. DOI:
 1238 [10.1016/j.astropartphys.2009.02.004](https://doi.org/10.1016/j.astropartphys.2009.02.004).
- 1239 [31] E. N. Parker. Dynamics of the Interplanetary Gas and Magnetic Fields. *Astrophysical
 1240 Journal*, 128:664, Nov 1958. DOI: [10.1086/146579](https://doi.org/10.1086/146579).
- 1241 [32] Christopher T. Russell. The Solar Wind and Magnetospheric Dynamics. In *Corre-
 1242 lated Interplanetary and Magnetospheric Observations*, pages 3–47, Dordrecht, 1974.
 1243 Springer Netherlands. DOI: [10.1007/978-94-010-2172-2_1](https://doi.org/10.1007/978-94-010-2172-2_1).
- 1244 [33] M.J. Owens and R.J. Forsyth. The Heliospheric Magnetic Field. *Living Rev. Sol.
 1245 Phys.*, 10, Nov 2013. DOI: [10.12942/lrsp-2013-5](https://doi.org/10.12942/lrsp-2013-5).
- 1246 [34] A. J. Dessler. Solar wind and interplanetary magnetic field. *Reviews of Geophysics*,
 1247 5(1):1–41, 1967. DOI: [10.1029/RG005i001p00001](https://doi.org/10.1029/RG005i001p00001).
- 1248 [35] R Cowen. Voyager 1 has reached interstellar space. *Nature*, 2013. DOI: [10.1038/nature.2013.13735](https://doi.org/10.1038/nature.2013.13735).
- 1249 [36] NASA. Solar wind at voyager 1, 2012. Retrieved 16:20, July 20, 2022 from:
https://commons.wikimedia.org/wiki/File:Solar_wind_at_Voyager_1.png.
- 1250 [37] David H. Hathaway. The Solar Cycle. *Living Reviews in Solar Physics*, 7(1):1, Dec
 1251

- 1253 2010. DOI: [10.12942/lrsp-2010-1](https://doi.org/10.12942/lrsp-2010-1).
- 1254 [38] Carsten Jorgensen, Christoffer Karoff, Senthamizh Pavai Valliappan, and Rainer Arlt.
1255 Christian Horrebow's Sunspot Observations – I. Life and Published Writings. *Solar
1256 Physics*, Jun 2019. DOI: [10.1007/s11207-019-1465-z](https://doi.org/10.1007/s11207-019-1465-z).
- 1257 [39] Christoffer Karoff, Carsten Jorgensen, Senthamizh Pavai Valliappan, and Rainer Arlt.
1258 Christian Horrebow's Sunspot Observations – II. Construction of a Record of Sunspot
1259 Positions. *Solar Physics*, 294, Jun 2019. DOI: [10.1007/s11207-019-1466-y](https://doi.org/10.1007/s11207-019-1466-y).
- 1260 [40] Eddie Ross and William J. Chaplin. The behaviour of galactic cosmic ray intensity
1261 during solar activity cycle 24. *Solar Physics*, 294(1):8, Jan 2019. DOI: [10.1007/s11207-019-1397-7](https://doi.org/10.1007/s11207-019-1397-7).
- 1263 [41] EA Bogomolov, ND Lubyanaya, VA Romanov, SV Stepanov, and MS Shulakova. A
1264 stratospheric magnetic spectrometer investigation of the singly charged component
1265 spectra and composition of the primary and secondary cosmic radiation. In *International
1266 Cosmic Ray Conference*, volume 1, page 330, 1979.
- 1267 [42] R. L. Golden, S. Horan, B. G. Mauger, G. D. Badhwar, J. L. Lacy, S. A. Stephens,
1268 R. R. Daniel, and J. E. Zipse. Evidence for the existence of cosmic-ray antiprotons.
1269 *Phys. Rev. Lett.*, 43:1196–1199, Oct 1979. DOI: [10.1103/PhysRevLett.43.1196](https://doi.org/10.1103/PhysRevLett.43.1196).
- 1270 [43] M. Nozaki. BESS-Polar. *Nuclear Instruments and Methods in Physics Research
1271 Section B: Beam Interactions with Materials and Atoms*, 214:110–115, 2004. DOI:
1272 [10.1016/j.nimb.2003.08.005](https://doi.org/10.1016/j.nimb.2003.08.005).
- 1273 [44] T. Yoshida, A. Yamamoto, and J. et al. Mitchell. Bess-polar experiment. *Life sciences
1274 and space research*, 33(10):1755–1762, 2004. DOI: [10.1016/j.asr.2003.05.017](https://doi.org/10.1016/j.asr.2003.05.017).
- 1275 [45] K. Abe et al. Measurement of the cosmic-ray low-energy antiproton spectrum with
1276 the first BESS-Polar Antarctic flight. *Physics Letters B*, 670(2):103–108, 2008. DOI:
1277 [10.1016/j.physletb.2008.10.053](https://doi.org/10.1016/j.physletb.2008.10.053).
- 1278 [46] K. Abe et al. Measurement of the Cosmic-Ray Antiproton Spectrum at Solar Minimum
1279 with a Long-Duration Balloon Flight over Antarctica. *Phys. Rev. Lett.*, 108:051102,
1280 Jan 2012. DOI: [10.1103/PhysRevLett.108.051102](https://doi.org/10.1103/PhysRevLett.108.051102).
- 1281 [47] A M Galper et al. The PAMELA experiment: a decade of Cosmic Ray Physics in space.
1282 *Journal of Physics: Conference Series*, 798:012033, Jan 2017. DOI: [10.1088/1742-6596/798/1/012033](https://doi.org/10.1088/1742-
1283 6596/798/1/012033).
- 1284 [48] O. Adriani et al. (PAMELA Collaboration). New Measurement of the Antiproton-to-Proton
1285 Flux Ratio up to 100 GeV in the Cosmic Radiation. *Phys. Rev. Lett.*, 102:051101, Feb 2009. DOI:
1286 [10.1103/PhysRevLett.102.051101](https://doi.org/10.1103/PhysRevLett.102.051101).

- 1287 [49] O. Adriani et al. (PAMELA Collaboration). PAMELA Results on the Cosmic-Ray Anti-
 1288 proton Flux from 60 MeV to 180 GeV in Kinetic Energy. *Phys. Rev. Lett.*, 105:121101,
 1289 Sep 2010. DOI: [10.1103/PhysRevLett.105.121101](https://doi.org/10.1103/PhysRevLett.105.121101).
- 1290 [50] M. Aguilar et al. (AMS Collaboration). Antiproton Flux, Antiproton-to-Proton Flux
 1291 Ratio, and Properties of Elementary Particle Fluxes in Primary Cosmic Rays Measured
 1292 with the Alpha Magnetic Spectrometer on the International Space Station. *Phys. Rev.
 1293 Lett.*, 117:091103, Aug 2016. DOI: [10.1103/PhysRevLett.117.091103](https://doi.org/10.1103/PhysRevLett.117.091103).
- 1294 [51] S. et al. Ahlen. An antimatter spectrometer in space. *Nuclear Instruments and Methods
 1295 in Physics Research Section A: Accelerators, Spectrometers, Detectors and Associated
 1296 Equipment*, 350(1):351–367, 1994. DOI: [10.1016/0168-9002\(94\)91184-3](https://doi.org/10.1016/0168-9002(94)91184-3).
- 1297 [52] Roberto Battiston. The antimatter spectrometer (AMS-02): A particle physics detector
 1298 in space. *Nuclear Instruments and Methods in Physics Research Section A: Accelerators,
 1299 Spectrometers, Detectors and Associated Equipment*, 588(1):227–234, 2008.
 1300 DOI: [10.1016/j.nima.2008.01.044](https://doi.org/10.1016/j.nima.2008.01.044).
- 1301 [53] M Aguilar et al. The Alpha Magnetic Spectrometer (AMS) on the International Space
 1302 Station: Part I - results from the test flight on the space shuttle. *Physics Reports*,
 1303 366(6):331–405, 2002. DOI: [10.1016/S0370-1573\(02\)00013-3](https://doi.org/10.1016/S0370-1573(02)00013-3).
- 1304 [54] Roskosmos. STS-91 PLB, 1998. Retrieved 16:20, July 20, 2022 from:
 1305 https://commons.wikimedia.org/wiki/File:STS-91_PLB.jpg.
- 1306 [55] NASA/Crew-2. View of the ISS taken during crew-2 flyaround
 1307 (iiss066-e-081311), 2021. Retrieved 16:20, July 20, 2022 from:
 1308 [https://commons.wikimedia.org/wiki/File:View_of_the_ISS_taken_during_Crew-2_flyaround_\(ISS066-E-081311\).jpg](https://commons.wikimedia.org/wiki/File:View_of_the_ISS_taken_during_Crew-2_flyaround_(ISS066-E-081311).jpg).
- 1310 [56] Zoe Budrikis. A decade of AMS-02. *Nature Reviews Physics*, 3(5):308–308, Jan 2021.
 1311 DOI: [10.1038/s42254-021-00320-7](https://doi.org/10.1038/s42254-021-00320-7).
- 1312 [57] Fabian Machate. *Study for large acceptance electron analysis with the Alpha Mag-
 1313 netic Spectrometer on the International Space Station*. Dissertation, RWTH Aachen
 1314 University, Aachen, 2021. DOI: [10.18154/RWTH-2021-09976](https://doi.org/10.18154/RWTH-2021-09976).
- 1315 [58] AMS Collaboration. The Alpha Magnetic Spectrometer on the International Space
 1316 Station, 2022. URL: <https://ams02.space>.
- 1317 [59] V. L. Ginzburg and I. M. Frank. Radiation of a uniformly moving electron due to its
 1318 transition from one medium into another. *J. Phys. (USSR)*, 9:353–362, 1945.
- 1319 [60] M. Heil et al. Operations and Alignment of the AMS-02 Transition Radiation De-
 1320 tector. In *33rd International Cosmic Ray Conference*, page 1232, 2013. URL:

- 1321 <https://galprop.stanford.edu/elibrary/icrc/2013/papers/icrc2013-1232.pdf>.
- 1322 [61] T. Siedenburg. The AMS TRD. A gasdetector designed for operation in
1323 space. *Nuclear Physics B - Proceedings Supplements*, 150:30–33, 2006. DOI:
1324 [10.1016/j.nuclphysbps.2004.06.001](https://doi.org/10.1016/j.nuclphysbps.2004.06.001).
- 1325 [62] Thomas Kirn. The AMS-02 TRD on the international space station. *Nuclear Instru-*
1326 *ments and Methods in Physics Research Section A: Accelerators, Spectrometers, Detec-*
1327 *tors and Associated Equipment*, 706:43–47, 2013. DOI: [10.1016/j.nima.2012.05.010](https://doi.org/10.1016/j.nima.2012.05.010).
- 1328 [63] Jerzy Neyman, Egon Sharpe Pearson, and Karl Pearson. Ix. On the problem of the
1329 most efficient tests of statistical hypotheses. *Philosophical Transactions of the Royal*
1330 *Society of London. Series A, Containing Papers of a Mathematical or Physical Char-*
1331 *acter*, 231(694-706):289–337, 1933. DOI: [10.1098/rsta.1933.0009](https://doi.org/10.1098/rsta.1933.0009).
- 1332 [64] B. Blau, S.M. Harrison, H. Hofer, S.R. Milward, J.S.H. Ross, S.C.C. Ting, J. Ulbricht,
1333 and G. Viertel. The superconducting magnet of ams-02. *Nuclear Physics B - Proceed-*
1334 *ings Supplements*, 113(1):125–132, 2002. DOI: [10.1016/S0920-5632\(02\)01831-5](https://doi.org/10.1016/S0920-5632(02)01831-5).
- 1335 [65] K. Lubelsmeyer et al. Upgrade of the Alpha Magnetic Spectrometer (AMS-02) for
1336 long term operation on the International Space Station (ISS). *Nuclear Instruments*
1337 *and Methods in Physics Research Section A: Accelerators, Spectrometers, Detectors*
1338 *and Associated Equipment*, 654(1):639–648, 2011. DOI: [10.1016/j.nima.2011.06.051](https://doi.org/10.1016/j.nima.2011.06.051).
- 1339 [66] Pierre Erwan Saouter. Operation and Performance of AMS-02 Silicon Tracker. *PoS*,
1340 Vertex2014:028, 2015. DOI: [10.22323/1.227.0028](https://doi.org/10.22323/1.227.0028).
- 1341 [67] Sadakazu Haino. Performance of the AMS-02 silicon tracker in the ISS mission. *Nucl.*
1342 *Instrum. Meth. A*, 699:221–224, 2013. DOI: [10.1016/j.nima.2012.05.060](https://doi.org/10.1016/j.nima.2012.05.060).
- 1343 [68] G. Ambrosi et al. Alignment of the AMS-02 Silicon Tracker. In
1344 *33rd International Cosmic Ray Conference*, page 1260, 2013. URL:
1345 <https://ui.adsabs.harvard.edu/abs/2013ICRC...33..570A>.
- 1346 [69] B. Alpat et al. The internal alignment and position resolution of the ams-02 sili-
1347 con tracker determined with cosmic-ray muons. *Nuclear Instruments and Methods in*
1348 *Physics Research Section A: Accelerators, Spectrometers, Detectors and Associated*
1349 *Equipment*, 613(2):207–217, 2010. DOI: [10.1016/j.nima.2009.11.065](https://doi.org/10.1016/j.nima.2009.11.065).
- 1350 [70] V. Bindi et al. Calibration and performance of the AMS-02 time of flight detector in
1351 space. *Nucl. Instrum. Meth. A*, 743:22–29, 2014. DOI: [10.1016/j.nima.2014.01.002](https://doi.org/10.1016/j.nima.2014.01.002).
- 1352 [71] V. Bindi, A. Contin, N. Masi, A. Oliva, F. Palmonari, L. Quadrani, and A. Tiseni. The
1353 time of flight detector of the AMS-02 experiment on the international space station.
1354 *Nucl. Instrum. Meth. A*, 718:478–480, 2013. DOI: [10.1016/j.nima.2012.11.061](https://doi.org/10.1016/j.nima.2012.11.061).

- 1355 [72] V. Bindi, E. Choumilov, A. Contin, N. Masi, A. Oliva, F. Palmonari, L. Quadrani, and Q. Yan. The AMS-02 Time of Flight (TOF) System: Construction
 1356 and Overall Performances in Space. In *International Cosmic Ray Conference*, volume 33 of *International Cosmic Ray Conference*, page 2298, Jan 2013. URL:
 1357 <https://ui.adsabs.harvard.edu/abs/2013ICRC...33.2298B>.
- 1360 [73] Hu Liu, J. Casaus, F. Giovacchini, A. Oliva, and X. Xia. The RICH detector of
 1361 AMS-02: 5 years of operation in space. *Nucl. Instrum. Meth. A*, 876:5–8, 2017. DOI:
 1362 [10.1016/j.nima.2016.12.011](https://doi.org/10.1016/j.nima.2016.12.011).
- 1363 [74] R. Pereira. The AMS-02 RICH detector: Performance during ground-based
 1364 data taking at CERN. *Nucl. Instrum. Meth. A*, 639:37–41, 2011. DOI:
 1365 [10.1016/j.nima.2010.09.036](https://doi.org/10.1016/j.nima.2010.09.036).
- 1366 [75] F. Giovacchini, J. Casaus, and A. Oliva. The AMS-02 RICH detector: Status and
 1367 physics results. *Nuclear Instruments and Methods in Physics Research Section A: Accelerators, Spectrometers, Detectors and Associated Equipment*, 952:161797, 2020.
 1368 DOI: [10.1016/j.nima.2019.01.024](https://doi.org/10.1016/j.nima.2019.01.024).
- 1370 [76] F. Giovacchini. Performance in space of the AMS-02 RICH detector. *Nuclear Instruments and Methods in Physics Research Section A: Accelerators, Spectrometers, Detectors and Associated Equipment*, 766:57–60, 2014. DOI: [10.1016/j.nima.2014.04.036](https://doi.org/10.1016/j.nima.2014.04.036).
- 1373 [77] Sylvie Rosier-Lees. Performance of the AMS02 electromagnetic calorimeter in space.
 1374 *J. Phys. Conf. Ser.*, 404:012034, 2012. DOI: [10.1088/1742-6596/404/1/012034](https://doi.org/10.1088/1742-6596/404/1/012034).
- 1375 [78] M. Vecchi et al. The electromagnetic calorimeter of the AMS-02 experiment. In
 1376 *Semaine de l’Astrophysique Francaise (SF2A 2012)*, Nice, France, Jun 2012. URL:
 1377 <http://hal.in2p3.fr/in2p3-00745677>.
- 1378 [79] C. Adloff et al. The AMS-02 lead-scintillating fibres Electromagnetic Calorimeter.
 1379 *Nucl. Instrum. Meth. A*, 714:147–154, 2013. DOI: [10.1016/j.nima.2013.02.020](https://doi.org/10.1016/j.nima.2013.02.020).
- 1380 [80] Marco Incagli. Performance of the AMS-02 Electromagnetic Calorimeter in Space.
 1381 *PoS*, TIPP2014:025, 2014. DOI: [10.22323/1.213.0025](https://doi.org/10.22323/1.213.0025).
- 1382 [81] Manuela Vecchi, Kaiyuan Wu, and Yuan-Hann Chang. A 3-dimensional electromagnetic
 1383 shower characterization and its application to AMS-02 pointing capability. In
 1384 *33rd International Cosmic Ray Conference*, page 0653, 2013.
- 1385 [82] Stefano Di Falco. Results of 2007 test beam of AMS-02 Electromagnetic Calorimeter.
 1386 *Adv. Space Res.*, 45:112–122, 2010. DOI: [10.1016/j.asr.2009.08.005](https://doi.org/10.1016/j.asr.2009.08.005).
- 1387 [83] G Gallucci and (for the AMS-02 ECAL group). Performance of the AMS-02 Electromagnetic
 1388 Calorimeter in Space. *Journal of Physics: Conference Series*, 587:012028,

- 1389 Feb 2015. DOI: [10.1088/1742-6596/587/1/012028](https://doi.org/10.1088/1742-6596/587/1/012028).
- 1390 [84] Ph. von Doetinchem, W. Karpinski, Th. Kirn, K. Luebelsmeyer, St. Schael, and
1391 M. Wlochal. The AMS-02 Anticoincidence Counter. *Nucl. Phys. B Proc. Suppl.*,
1392 197:15–18, 2009. DOI: [10.1016/j.nuclphysbps.2009.10.025](https://doi.org/10.1016/j.nuclphysbps.2009.10.025).
- 1393 [85] T. Bruch and W. Wallraff. The Anti-Coincidence Counter shield of the AMS tracker.
1394 *Nucl. Instrum. Meth. A*, 572:505–507, 2007. DOI: [10.1016/j.nima.2006.10.376](https://doi.org/10.1016/j.nima.2006.10.376).
- 1395 [86] A. Basili, V. Bindi, D. Casadei, G. Castellini, A. Contin, A. Kounine, M. Lolli, F. Pal-
1396 monari, and L. Quadrani. The TOF-ACC flight electronics for the fast trigger and time
1397 of flight of the AMS-02 cosmic ray spectrometer. *Nucl. Instrum. Meth. A*, 707:99–113,
1398 2013. DOI: [10.1016/j.nima.2012.12.089](https://doi.org/10.1016/j.nima.2012.12.089).
- 1399 [87] Ph. von Doetinchem, Th. Kirn, K. Luebelsmeyer, and St. Schael. The Anticoincidence
1400 Counter System of AMS-02, 2009. DOI: [10.48550/ARXIV.0906.1068](https://arxiv.org/abs/0906.1068).
- 1401 [88] Rene Brun and Fons Rademakers. Root - An object oriented data analysis frame-
1402 work. *Nuclear Instruments and Methods in Physics Research Section A: Accelerators,*
1403 *Spectrometers, Detectors and Associated Equipment*, 389(1):81–86, 1997. DOI:
1404 [10.1016/S0168-9002\(97\)00048-X](https://doi.org/10.1016/S0168-9002(97)00048-X).
- 1405 [89] Bastian Beischer. *Measurement of high energy gamma rays from 200 MeV to 1 TeV*
1406 *with the Alpha Magnetic Spectrometer on the International Space Station*. Dissertation,
1407 RWTH Aachen University, Aachen, 2020. DOI: [10.18154/RWTH-2020-06535](https://doi.org/10.18154/RWTH-2020-06535).
- 1408 [90] M. Aguilar et al. (AMS Collaboration). Precision Measurement of the Proton Flux
1409 in Primary Cosmic Rays from Rigidity 1 GV to 1.8 TV with the Alpha Magnetic
1410 Spectrometer on the International Space Station. *Phys. Rev. Lett.*, 114:171103, Apr
1411 2015. DOI: [10.1103/PhysRevLett.114.171103](https://doi.org/10.1103/PhysRevLett.114.171103).
- 1412 [91] J. Bartels. Twenty-seven day recurrences in terrestrial-magnetic and solar activity,
1413 1923–1933. *Terrestrial Magnetism and Atmospheric Electricity*, 39(3):201–202a, 1934.
1414 DOI: [10.1029/TE039i003p00201](https://doi.org/10.1029/TE039i003p00201).
- 1415 [92] S. Agostinelli et al. GEANT4—a simulation toolkit. *Nucl. Instrum. Meth. A*, 506:250–
1416 303, 2003. DOI: [10.1016/S0168-9002\(03\)01368-8](https://doi.org/10.1016/S0168-9002(03)01368-8).
- 1417 [93] J. Allison et al. Recent developments in Geant4. *Nucl. Instrum. Meth. A*, 835:186–225,
1418 2016. DOI: [10.1016/j.nima.2016.06.125](https://doi.org/10.1016/j.nima.2016.06.125).
- 1419 [94] Paolo Zuccon. AMS-02 Track reconstruction and rigidity measurement. In *33rd Inter-*
1420 *national Cosmic Ray Conference*, page 1064, 2013. URL: [https://s3.cern.ch/inspire-
1421 prod-files-7/71c48c76263c1f7bee2621c779ba3320](https://s3.cern.ch/inspire-prod-files-7/71c48c76263c1f7bee2621c779ba3320).

- 1422 [95] Helge Voss, Andreas Hocker, Jorg Stelzer, and Fredrik Tegenfeldt. TMVA, the toolkit
1423 for multivariate data analysis with ROOT. In XI International Workshop on Advanced
1424 Computing and Analysis Techniques in Physics Research, volume 50, page 040. SISSA
1425 Medialab, 2009. DOI: [10.22323/1.050.0040](https://doi.org/10.22323/1.050.0040).
- 1426 [96] J.D. Sullivan. Geometric factor and directional response of single and multi-element
1427 particle telescopes. *Nuclear Instruments and Methods*, 95(1):5–11, 1971. DOI:
1428 [10.1016/0029-554X\(71\)90033-4](https://doi.org/10.1016/0029-554X(71)90033-4).
- 1429 [97] Nikolas Zimmermann. *Precision measurement of the cosmic-ray electron and positron*
1430 *fluxes as a function of time and energy with the Alpha Magnetic Spectrometer on the*
1431 *International Space Station*. Dissertation, RWTH Aachen University, Aachen, 2020.
1432 DOI: [10.18154/RWTH-2020-02650](https://doi.org/10.18154/RWTH-2020-02650).
- 1433 [98] Carl Stormer. The polar aurora. *Quarterly Journal of the Royal Meteorological Society*,
1434 82(351):115–115, 1956. DOI: [10.1002/qj.49708235123](https://doi.org/10.1002/qj.49708235123).
- 1435 [99] G. D’Agostini. A multidimensional unfolding method based on Bayes’ theorem. *Nu-*
1436 *clear Instruments and Methods in Physics Research Section A: Accelerators, Spectrom-*
1437 *eters, Detectors and Associated Equipment*, 362(2):487–498, 1995. DOI: [10.1016/0168-9002\(95\)00274-X](https://doi.org/10.1016/0168-9002(95)00274-X).
- 1439 [100] Tim Adye. Unfolding algorithms and tests using RooUnfold. In *PHYSTAT 2011*,
1440 pages 313–318, Geneva, 2011. CERN. DOI: [10.5170/CERN-2011-006.313](https://doi.org/10.5170/CERN-2011-006.313).
- 1441 [101] AMS Collaboration. The Alpha Magnetic Spectrometer (AMS) on the international
1442 space station: Part II – Results from the first seven years. *Physics Reports*, 894:1–116,
1443 2021. DOI: [10.1016/j.physrep.2020.09.003](https://doi.org/10.1016/j.physrep.2020.09.003).